Dynamic Capillary Effects in the Simulation of Flow and Transport in Porous Media: A New Linearisation Method

Master's Thesis in Applied and Computational Mathematics

Silje Kjønaas Teveldal

Department of Mathematics
University of Bergen

December 25, 2014

Acknowledgements

First and foremost I would like to extend my everlasting gratitude towards my supervisor Florin A. Radu. Thank you for your excellent guidance and advice, as well as your never-ending patience when I come to you for help. I greatly appreciate the opportunities to travel as part of my degree thanks to your dedication and initiative.

A special thanks to Florian Doster for his input and helpful advice, as well as the rest of the people at the Institute of Petroleum Engineering at Heriot-Watt University in Edinburgh. Their generous hospitality made my stay both educational and memorable.

Thanks to all my friends, especially the ones I have made along the way, for making my time at university the best time of my life yet. Also, I am forever grateful for my wonderful family and boyfriend for standing by me and always lending their support.

Last but not least, I would like to pay tribute to all the fantastic teachers and lecturers I have had over the years whose inspiration has been invaluable in my choice to pursue a degree in mathematics.

Silje Kjønaas Teveldal,
December 2014

Abstract

In this thesis mathematical models with and without dynamic capillary effects are developed to model water flow and solute transport through a porous medium. The system of equations are discretised using the finite volume method TPFA in space and the backward Euler method in time. To solve the nonlinear systems appearing at each time step numerically, robust linearisation methods are proposed. These methods do not involve the computation of derivatives. The methods are analysed and have been shown to be linearly convergent and robust. Moreover, the convergence was shown to be independent of mesh size. The influence that the dynamic effects have on flow and transport is studied numerically. Additional numerical experiments were conducted to study the convergence of the linearisation schemes. The numerical results are shown to be in correspondence with the theoretical results.

Contents

Acknowledgements **iii**

Abstract **v**

1 Introduction **1**

2 Mathematical Modelling of Porous Media Flow **3**
2.1 Flow in Porous Media . . . 3
2.1.1 Physical Properties . . . 4
2.1.2 Fluid Properties . . . 6
2.1.3 Darcy's Law . . . 6
2.1.4 Mass Conservation . . . 9
2.1.5 Diffusion and Transport Equations . . . 11
2.2 Two-Phase Flow Model . . . 12
2.2.1 Two-Phase Flow . . . 13
2.2.2 Capillary Pressure . . . 13
2.2.3 Richards' Equation . . . 14
2.2.4 Parameterisations . . . 15
2.3 Non-Standard Models . . . 16
2.3.1 Dynamic Capillary Pressure and Hysteresis . . . 16
2.3.2 Extension of the Standard Model . . . 18
2.4 The Mathematical Model . . . 20
2.4.1 Simplifications of the Mathematical Model . . . 20
2.4.2 Representative Equations . . . 20

3 Numerical Methods **23**
3.1 Grid . . . 23
3.2 Discretisation in Space . . . 25
3.2.1 Finite Difference Method . . . 26
3.2.2 TPFA . . . 27
3.2.3 Boundary Conditions . . . 31
3.3 Discretisation in Time . . . 35
3.4 Linearisation . . . 36
3.4.1 Linearisation Richards . . . 37

3.4.2 Linearisation Dynamic Capillary Pressure 40
3.5 Discretisation in Space and Time 43
3.5.1 Convection-Diffusion Equation 44
3.5.2 Standard Richards' Equation 47
3.5.3 Richards' Equation with Dynamic Capillary Pressure 50
3.6 Implementation 52

4 Numerical Results **55**
4.1 Convergence for an Academical Example 55
4.2 Numerical Simulations 58
4.2.1 Numerical Solutions of Flow and Transport 59
4.2.2 Convergence History of the Linearisation Schemes 69

5 Conclusion **75**

Chapter 1

Introduction

A classic case of gravity-driven flow in porous media is infiltration of water through soil. An important application connected to this is the pollution of groundwater. Organic compounds deposited on the ground surface or being used at i.e. chemical factories, enter the soil and through infiltration of water containing the dissolved substances these contaminants can reach the groundwater. Stability of the flow field is a key question for the infiltration, as the formation of what is known as preferential flow paths can create large consequences on the transport of contaminants to ground and surface waters. It has been shown through experiments that the instability is related to a phenomena in one dimensional infiltrations called saturation or pressure overshoot [9].

Through experimental evidence presented in [18] it was suggested that hysteresis and dynamic effects in the capillary pressure relationship represent an important role and have the potential of describing phenomena of saturation overshoot and preferential flow paths. In order to evaluate the safety connected to a contaminated site, a reliable prediction of the water movement and solute transport is of key importance. So to model the water flow the Richards equation will be used. However, when this equation is based on the static relation for the capillary pressure, given by $p_c = p_a - p_w$, it is unable to predict unstable infiltrations. Thus, mathematical models including dynamic or non-equilibrium effects will be considered.

Robust and flexible numerical methods are needed to successfully handle these conditions. To recognise the most optimal numerical methods, a set of conditions the methods should satisfy are introduced. Such conditions include the principle of mass conservation as well as the method's ability to yield explicit expressions for the fluid flux inside the medium at a lowest possible CPU time. The finite

volume method TPFA satisfies these conditions, while the classical methods such as finite difference (FD) and finite element method (FEM) are not optimal with regards to these conditions [19].

In this thesis the TPFA method will be used for the spatial discretisation and the backward Euler method for the temporal discretisation. On each time step a nonlinear system of equations arises. In order to solve this system numerically a linearisation scheme is needed. A common method for solving such systems is Newton's method. However, two main concerns regarding the Newton method is that the Jacobian of the system has to be assembled, as well as the fact that the convergence of the method is not guaranteed when the initial guess is not "close enough" to the solution, implying a restriction on the time step.

Therefore, to treat the nonlinearities of the PDEs in the mathematical models, two linearisation schemes will be proposed and analysed. The first scheme applies to the standard Richards equation and is based on the works presented in [37] and [36]. It is in this thesis applied for the TPFA method for the first time. The second linearisation scheme applies to Richards' equation with dynamic capillarity. It continues the works in [36, 37]. The scheme is new. The linearisation schemes do not involve the computation of derivatives and will be shown to be very robust. Moreover, the convergence of the schemes is independent of the mesh diameter, this being an important advantage when compared to other linearisation methods.

The outline of this thesis is set up in the following way. In **Chapter 2** representative mathematical models will be developed to describe flow and transport in porous media. **Chapter 3** gives an introduction to the numerical methods used to solve the system of equations. The equations are discretised using the TPFA and backward Euler method. Additionally, to treat the nonlinearities of the model equations, two numerical linearisation methods are proposed and the convergence analysis is presented. Further, numerical simulations are conducted and the numerical results are then presented in **Chapter 4**. Here, the flow and transport profiles as well as the convergence of the linearisation schemes will be evaluated numerically. The conclusion is given in **Chapter 5**.

Chapter 2

Mathematical Modelling of Porous Media Flow

This chapter is devoted to giving an overview of the equations describing flow in porous media. Through discussion of the physical properties of the fluids and the porous medium, the background for the mathematical model will be provided and the governing equations used to model contaminant transport will be presented. Further, to account for possible dynamic effects related to the phenomena of saturation overshoot and the origination of preferential flow paths, certain extensions of the standard model will be given. To conclude the chapter, some assumptions in order to simplify the model will be presented and a summary of the main equations throughout the chapter is made. The aim of this chapter is thus to present and explain the equations needed to construct the representative mathematical models which are used in the numerical methods discussed later in the thesis.

2.1 Flow in Porous Media

Several important properties of the fluid and the porous medium has to be taken into consideration when deriving the mathematical model. These properties, as well as the main equations for describing flow in porous media, being Darcy's law and equations of mass conservation, will be presented in the following.

2.1.1 Physical Properties of a Porous Medium

The focus of this thesis includes the transport of contaminants through soil, which can be defined as a porous medium. However, soil is merely one example in a vast group of porous materials and domains ranging from lungs and kidneys to groundwater aquifers and oil reservoirs. A common factor in all these examples is that part of the domain is occupied by the solid matrix, while the remaining part known as the void space consists of pores. The pores in a porous medium are occupied either by a single fluid phase, or by multiple fluid phases, e.g., gas, water and oil, with each phase occupying a distinct portion of the void space [1].

Flow pathways exist within the pore space of the material, often consisting of a complex structure of both interconnected and isolated pores. The fine scale of these flow paths cannot reasonably be resolved, instead averages over length scales more convenient are defined. The scale of choice is referred to as a *representative elementary volume* (REV) [2]. Then to one mathematical point in space, within the porous medium, the properties of the REV surrounding this point is associated, see Figure 2.1.

The length scale of the REV typically range from one centimetre to a few tens of centimetres, and is large enough to allow for meaningful averages of the void space and solid matrix to be defined and laboratory measurements to be made [2]. This is known as the *continuum approach* and is recognized for its ability in preserving heterogeneities in the medium even though an exact small-scale representation of the pores is not obtained [14].

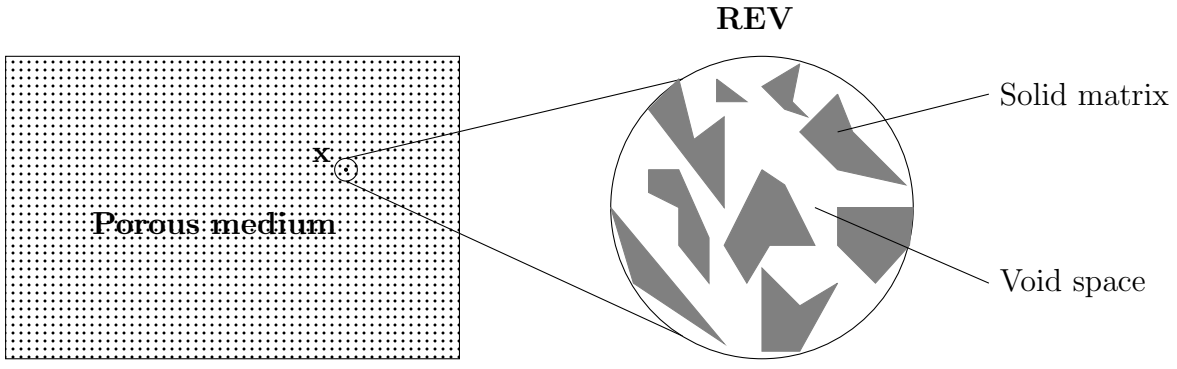

FIGURE 2.1: The representative elementary volume (REV) of point $\mathbf{x}$ in space of a porous medium.

Let Ω denote the REV. By expressing the void space volume as Ω_v and the solid matrix volume as Ω_s, so that

$$\Omega = \Omega_v + \Omega_s, \tag{2.1}$$

the porosity can be defined as

$$\phi = \frac{\Omega_v}{\Omega}. \tag{2.2}$$

In other words, the porosity is the ratio between the volume of the voids in the REV and the total volume of the REV.

Below the ground surface the domain is commonly divided into a saturated zone and an unsaturated zone. The two zones are separated by the water table, where the pressure head is equal to the atmospheric pressure [13]. In the saturated zone all available pores are filled with water, while in the unsaturated zone this is not the case. Hence, there are two phases present in the void space of the unsaturated zone. These are water and air. When dealing with two-phase flow, the need to indicate the fraction of the pore space occupied by each fluid develops. Denoting Ω_w and Ω_a as the volume occupied by water and air respectively, the fraction of water, also known as *water saturation*, is given by

$$S_w = \frac{\Omega_w}{\Omega_v}, \tag{2.3}$$

and the fraction of air by

$$S_a = \frac{\Omega_a}{\Omega_v}. \tag{2.4}$$

Since the sum of the volumes occupied by water and air equals the void space volume

$$\Omega_v = \Omega_w + \Omega_a, \tag{2.5}$$

the sum of the water saturation and the air fraction equals one

$$S_w + S_a = 1. \tag{2.6}$$

From this, the water content θ can be defined as the volume of water divided by the total volume of the REV. It is given by the porosity ϕ, multiplied with the water saturation S_w

$$\theta_w = S_w\phi = \frac{\Omega_w}{\Omega_v}\frac{\Omega_v}{\Omega} = \frac{\Omega_w}{\Omega}. \tag{2.7}$$

2.1.2 Fluid Properties

Viscosity of a fluid, μ, and *density* of a fluid, ρ, are two important properties in the modelling of flow in porous media. The *viscosity* is a measure of internal friction within a phase, and describes the phases' resistance to flow [14]. Meaning, the higher the value - the slower the flow.

The *density* is defined as the ratio between mass and volume of a fluid

$$\rho = \frac{\text{Mass of fluid}}{\text{Volume of fluid}}. \tag{2.8}$$

For a given temperature, T, the density of a fluid is normally dependent on the pressure, p, applied to the fluid. Therefore, in practice, a fluid is usually *compressible*.

2.1.3 Darcy's Law

First published by Henry Darcy in 1856, Darcy's law is one of the most important building blocks for the description of flow in porous media [2]. The basis of the relation was formed by the study of empirical experiments related to water treatment and the design of sand filters (detailed explanation of the experiments in [2] p.17-19). It is worth noting, that due to friction between the phase and the wall of the pore being a dominating factor for flow in pores, the hydrodynamic flow equations, e.g. the Navier-Stokes equation, cannot be used to model flow in a porous medium [3].

From his experiments, Darcy found that the volumetric flow rate q is proportional to the cross-sectional area A, the difference in hydraulic head h, and inversely proportional to the distance between the measurement points l [2]. Giving,

$$q \sim \frac{A(h_2 - h_1)}{l}. \tag{2.9}$$

By including the hydraulic conductivity κ, and dividing by the area A, eq. (2.9) can be expressed as the volumetric flux u of water through the column

$$u \equiv \frac{q}{A} = \frac{\kappa(h_2 - h_1)}{l}. \tag{2.10}$$

The relation was later derived mathematically [2].

Introducing $h = \frac{p}{\rho g} + z$ and $k = \frac{\kappa\mu}{\rho g}$, the extension of Darcy's law into a differential equation yields

$$\mathbf{u} = -\frac{\kappa}{\rho g}\nabla(p + \rho g z) = -\frac{k}{\mu}(\nabla p - \rho \mathbf{g}), \tag{2.11}$$

where k is the permeability, μ the fluid viscosity, p the pressure, ρ the fluid density, $\mathbf{g}$ is the gravitational acceleration and z the height against the gravitational direction. The gradient of the hydraulic head represents the fluids ability to flow at a given spatial point in the porous medium.

The hydraulic head, h, is found by examining the state of water in the porous medium, which is described by its energy [13]. From elementary physics, recall that

$$\text{Energy} = \text{Kinetic Energy} + \text{Potential Energy}. \tag{2.12}$$

Assuming the flow to be a so-called *laminar flow*, meaning the flow of water being sufficiently slow, the kinetic energy may be neglected. Additionally, by disregarding the influence on the flow by all other factors than the pressure and gravitational forces acting on the fluid, the potential energy at a given spatial point in the porous medium may be written as

$$\text{Potential Energy} = \text{Pressure Potential} + \text{Gravitational Potential}. \tag{2.13}$$

The potential energy of a fluid in a porous medium is often called the *hydraulic potential* [13]. By inserting the formulas for the potentials into eq. (2.13), the following equation is obtained

$$mgh = pV + mgz. \tag{2.14}$$

Here m is the mass of the fluid, V the volume, p is the pressure on the fluid at the spatial point being considered and z the elevation from a reference level called *datum*. Manipulations of eq. (2.14) gives the formula describing hydraulic head

$$h = \frac{pV}{mg} + z = \frac{p}{\rho g} + z. \tag{2.15}$$

The second equality holds from the fact that $\rho = \frac{m}{V}$, and the minus sign in Darcy's law is added since a fluid in a porous medium flows from higher values to lower values of hydraulic head.

The permeability k is another important property of the porous medium [2]. It measures the ability of the porous medium to transmit fluid, and is an average property of the medium [4]. Meaning, a porous medium with a large permeability has a higher ability to transmit fluid through its pore space than a porous medium with a small permeability. However, if the permeability is sufficiently close to zero the porous medium is so-called *impermeable*, which means that it does not transmit fluid through its pores [13].

An interesting aspect of flow in porous media is that the porous medium may allow a fluid to flow more easily in one direction than another [2]. Therefore, the concepts of *anisotropic* and *isotropic* material and *homogeneous* and *heterogeneous* material are important to derive for further understanding of the permeability. If the material making up the solid matrix of a porous medium is *anisotropic*, the permeability changes value depending on the direction being considered. If there are no directional differences in the permeability, the material is said to be *isotropic*. When the permeability changes as a function of spatial location, the material is referred to as *heterogeneous*. Conversely, when a material is spatially uniform, it is called *homogeneous* [2]. For homogeneous and isotropic media, the permeability k is a constant scalar [3]. The medium considered in this thesis is assumed to be an isotropic, homogeneous medium.

Although there are two phases present in unsaturated soil, the interest in this thesis lies in modelling the flow of the water phase. The presence of the air phase does however influence the flow of water, seeing as the air phase occupies some of the pore space reducing the set of pores through which the water phase is able to flow. This results in an increase in difficulty in the fluid flow, which is reflected in a lower value of the apparent permeability [2]. To account for this reduction, the absolute permeability k in eq. (2.11) is multiplied with a relative permeability k_r, which is a function of volumetric occupancy of the fluids [2]. The relative permeability of the water phase depends on the water saturation

$$k_r = k_r(S_w), \tag{2.16}$$

whereas the absolute permeability k is a material parameter depending on the medium. The effective permeability for the water phase is given by

$$k_e = k_r(S_w)k, \tag{2.17}$$

which is a reduced permeability due to the presence of an air phase in addition to the water phase.

Darcy's law for the water phase is then given by,

$$\mathbf{u}_w = -\frac{k_r(S_w)k}{\mu_w}(\nabla p_w - \rho_w \mathbf{g}). \tag{2.18}$$

Here μ_w denotes water viscosity, ρ_w the water density and p_w the water pressure.

2.1.4 Mass Conservation

The mathematical statement of the principle of conservation of mass is another important building block when modelling flow in porous media. The basis for the equation of mass conservation is formed by the statement that the change of mass of a particular substance within a volume has to be equal to the amount of mass created inside the volume, minus the mass that leaves the volume through its boundaries [2]. In the following, the mass conservation equation will be derived in a similar fashion as in [5] and [2].

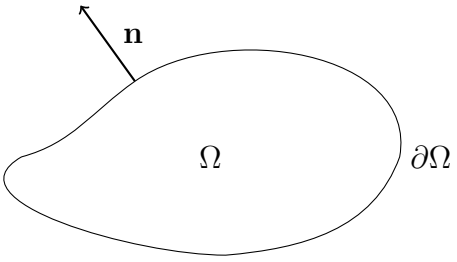

FIGURE 2.2: A domain Ω with boundary $\partial\Omega$ and outward unit normal $\mathbf{n}$

First, introducing an arbitrary volume Ω, with boundary $\partial\Omega$ and outward unit normal $\mathbf{n}$, see Figure 2.2. The mass per total volume of a species is given by the porosity ϕ times its density ρ. Then, the time variation of the total mass in Ω is given by

$$\frac{\partial}{\partial t}\int_\Omega \phi\rho \, dV. \tag{2.19}$$

Using Leibniz integral rule [6] this expression becomes

$$\int_\Omega \frac{\partial}{\partial t}(\phi\rho) \, dV. \tag{2.20}$$

For this derivative not to equal zero, there has to be a source or sink inside Ω or a flux through the boundary $\partial\Omega$. Both will be considered in the following.

The net flux over the boundary $\partial\Omega$ is given by

$$\int_{\partial\Omega} (\rho \mathbf{u}) \cdot \mathbf{n} \, dS, \tag{2.21}$$

where $\mathbf{u}$ is the volumetric flux vector and $\mathbf{n}$ denotes the outward unit normal to the surface $\partial\Omega$. Defining the source density Q, the total production or destruction is given by

$$\int_{\Omega} Q \, dV. \tag{2.22}$$

Collecting the previous terms (eqs. (2.20) to (2.22)), the mass conservation equation on integral form is described by

$$\int_{\Omega} \frac{\partial}{\partial t}(\phi\rho) \, dV + \int_{\partial\Omega} (\rho \mathbf{u}) \cdot \mathbf{n} \, dS = \int_{\Omega} Q \, dV. \tag{2.23}$$

To obtain the more general form of the mass conservation equation, the divergence theorem [6] is applied to the boundary integral, $\mathbf{u}$ is assumed to be sufficiently smooth and it is acknowledged that eq. (2.23) holds for any arbitrary closed volume Ω. Then, the differential form of the mass conservation equation is obtained

$$\frac{\partial}{\partial t}(\phi\rho) + \nabla \cdot (\rho \mathbf{u}) = Q. \tag{2.24}$$

As in the previous section covering Darcy's law, the mass conservation equation can be expressed for the water phase. Water being an immiscible fluid as it does not mix with air, the mass of the water phase is a conserved quantity, satisfying

$$\frac{\partial(\rho_w \phi_w S_w)}{\partial t} + \nabla \cdot (\rho_w \mathbf{u}_w) = Q_w. \tag{2.25}$$

Using that $\theta_w = \phi_w S_w$ the equation for the conservation of mass for the water phase is described by the following equation,

$$\frac{\partial \rho_w \theta_w}{\partial t} + \nabla \cdot (\rho_w \mathbf{u}_w) = Q_w. \tag{2.26}$$

$\mathbf{u}_w$ is the volumetric flux obtained from Darcy's law.

2.1.5 Diffusion and Transport Equations

The point of interest in this thesis lies not only in the overall fluid phase, but rather in the movement of one or more of the components that make up the phase in question, namely the water phase. More specifically, the transport of dissolved contaminants. Let $c = c(x,t)$ define the concentration of a component. The conservation equation for the component within the fluid phase can then be given as

$$\frac{\partial c}{\partial t} + \nabla \cdot \mathbf{J} = Q, \tag{2.27}$$

where $\mathbf{J}$ denotes the flux over the boundary $\partial\Omega$ of the domain Ω. Flux is a quantity defined on a "per area, per time" basis [2]. Q still denotes any sources or sinks.

A dissolved component may be transported by the means of advective transport or molecular diffusion. Advective transport is referred to as the transport by the bulk flow of the fluid phase, whereas for diffusion the fluid is at rest and the molecules move from areas of high concentration to areas of low concentration by random movements of the dissolved particles. Experimental evidence leads to the following law

$$\mathbf{J}^{(1)} = -D\nabla c \tag{2.28}$$

describing diffusion. Where D is the diffusion coefficient, also called molecular diffusivity [5]. Equation (2.28) is known as Fick's first law [7].

Inserting eq. (2.28) into eq. (2.27), the *diffusion equation* is obtained

$$\frac{\partial c}{\partial t} - \nabla \cdot (D\nabla c) = Q. \tag{2.29}$$

For a fluid in motion, convection of the particles takes place. This being described by

$$\mathbf{J}^{(2)} = \mathbf{u}c. \tag{2.30}$$

Here, $\mathbf{u}$ is the velocity of the fluid found by Darcy's law (eq. (2.11)). By taking both transport and diffusive processes into account, the *convection-diffusion equation* is obtained

$$\frac{\partial c}{\partial t} - \nabla \cdot (D\nabla c - \mathbf{u}c) = Q. \tag{2.31}$$

The relative strength between the two processes in eq. (2.31) is measured by the Péclet number [5]. One process may dominate the other, in which case the dominated process may be ignored and only the dominating process considered. I.e.,

if convection dominates, diffusion can be ignored, and the *transport equation* is considered

$$\frac{\partial c}{\partial t} + \nabla \cdot (\mathbf{u}c) = Q. \tag{2.32}$$

The diffusion equation, eq. (2.29), is a second order parabolic partial differential equation (PDE), while the transport equation, eq. (2.32), is a first order hyperbolic PDE [8]. Adaptive discretisation techniques will be necessary due to the fact that the different nature of the two processes has to be reflected in the model [5]. In this thesis, examples containing both diffusion and transport will be considered, hence the convection-diffusion equation will be applied.

As stated at the start of this section, transport of dissolved contaminants in the water phase, i.e. organic solvents, are of interest. By denoting a component within the fluid phase by subscript i, the concentration of the component is defined as the ratio of the mass of component i to the total mass of the fluid phase [2],[5]. The subscript is omitted in the following, due to the fact that only one component is assumed dissolved. Applying an averaging procedure, recalling that the water content is given by $\theta_w := S_w\phi$ and using a phenomenological description for the diffusive mass flux [5], the resulting differential equation for the water phase reads

$$\frac{\partial(\theta_w c)}{\partial t} - \nabla \cdot (\theta_w D\nabla c - \mathbf{u}_w c) = Q. \tag{2.33}$$

If the production rate Q is independent of c, eq. (2.33) is linear [5]. This is assumed true in later chapters. Equation (2.33) models transport through diffusion and convection of a dissolved substance.

2.2 Two-Phase Flow Model

When modelling flow through a porous medium such as soil, different considerations are necessary when encountering the saturated and the unsaturated zone. Recalling that the saturated zone is completely filled with the water phase, this relates to single-phase flow. However, in order to model flow through the unsaturated zone the need to develop the concept of two-phase flow emerges. This need originates from the fact that both a water and an air phase is present in this zone. To construct the two-phase flow model, which in this thesis is the simplified model known as the Richards equation, some important properties of two-phase flow has to be considered.

2.2.1 Two-Phase Flow

Modelling of two-phase flow in porous media, concerns the simultaneous flow of two fluid phases within a porous medium. Again, the two fluid phases in question being water and air. One of the phases is referred to as the *wetting phase*, while the other is referred to as the *nonwetting phase*. This is defined in such a way that the fluid which is preferentially attracted by the solid is called the wetting fluid, while the other fluid is referred to as the nonwetting fluid [2]. The contact angle is defined as the angle between the fluid-fluid interface and the solid, and is used to determine whether or not a fluid is a wetting or a nonwetting fluid. The fluid on the side of the interface with an angle less than 90° with respect to the solid surface is the wetting fluid [2].

In section 2.1.1, the saturation (S_α) for each fluid phase was defined. Here, α denotes either the wetting phase ($\alpha = \omega$) or the nonwetting phase ($\alpha = n$). For the porous medium soil, with water and air as the two phases present, water is the wetting fluid and air the nonwetting fluid. Hence, $\alpha = w, a$ is chosen to represent the water and air phase respectively.

2.2.2 Capillary Pressure

An important role in describing two-phase flow in a porous medium, is played by the existence of fluid-fluid interfaces at the pore scale. This allows the two fluids to coexist in the pore space. From the fact that these interfaces can support nonzero stresses, different pressures can exist on either side of the interphase [2]. Hence, each phase usually has a different pressure. The difference between the phase pressures is defined as the *capillary pressure*, denoted by p_c, and is defined by

$$p_a - p_w = p_c(S_w). \tag{2.34}$$

Here, p_a is the pressure of the air phase, while p_w represents the pressure of the water phase. The capillary pressure can be measured as a function of the water saturation S_w, and is a hysteretic function [9] which will be defined in section 2.3.1.

2.2.3 Richards' Equation

From a two-phase flow system, a simplified representation often used to describe water movement in unsaturated soils can be derived. This is the Richards equation. The applications of this equation are valid for a two-phase porous medium where the two phases are water and air. The domain of interest being the shallow soil zone whose top boundary corresponds to the land surface [2].

Some important properties allow for this simplification, the biggest and most important one being the assumption that the air phase is at constant pressure everywhere in the soil [13]. This assumption is based on other simplifications, which include rapid flow of air, meaning that air movements are driven by small pressure gradients, and that the domain is interconnected and connected to the exterior atmosphere [2].

Considering these simplifications yields an approach for deriving Richards' equation. The simple two-phase flow model for immiscible fluids is represented by the following set of equations

$$\frac{\partial \theta_\alpha}{\partial t} + \nabla \cdot (\mathbf{u}_\alpha) = \frac{Q_\alpha}{\rho_\alpha} = f_\alpha, \tag{2.35}$$

$$\mathbf{u}_\alpha = -\frac{k_{r,\alpha} k}{\mu_\alpha}(\nabla p_\alpha - \rho_\alpha \mathbf{g}), \tag{2.36}$$

$$S_w + S_a = 1, \tag{2.37}$$

$$p_a - p_w = p_c(S_w). \tag{2.38}$$

Recall, θ_α is the water content and $\mathbf{u}_\alpha$ the volumetric flux, with $\alpha = w, a$, representing the water and air phase respectively. Equation (2.35) is the mass conservation equation and holds because the density ρ_α is set to be constant. The second equation is the Darcy law, while eq. (2.37) is the relation given by eq. (2.6), see section 2.1.1. Equation (2.38) is the capillary pressure.

Since the air pressure is assumed to be equal to the atmospheric pressure everywhere, i.e. $p_a = 0$, this means that one of the primary unknowns is eliminated and one of the equations, this being the air-phase equation, can be eliminated [2]. The capillary pressure p_c is now equal to the negative of the water pressure p_w,

$$p_c(S_w) = -p_w. \tag{2.39}$$

The capillary pressure is positive because the water pressure is less than the atmospheric pressure in the unsaturated zone [2]. By expressing Darcy's law with

respect to the pressure head, $\Psi_w = \frac{p_w}{\rho_w g}$, and the height against the gravitational direction z,

$$\mathbf{u}_w = -K(\theta_w(\Psi_w))\nabla(\Psi_w + z), \tag{2.40}$$

where $K(\theta_w(\Psi_w))$ is the hydraulic conductivity and both K and θ are given functions of Ψ. This can be inserted into eq. (2.35) and hence give rise to what is defined as the Richards' equation,

$$\frac{\partial \theta_w(\Psi_w)}{\partial t} - \nabla \cdot [K(\theta_w(\Psi_w))\nabla(\Psi_w + z)] = f_w. \tag{2.41}$$

$\theta_w(\Psi_w)$ is obtained by inverting the relation given by eq. (2.39). Equation (2.41) is a nonlinear PDE consisting of the second derivative with respect to space and first derivative with respect to time. Thus, it is recognized as a *parabolic* PDE.

2.2.4 Parameterisations

As stated in section 2.2.3, the hydraulic conductivity K, and water content θ are known functions of the pressure head Ψ. Based on experimental results, different functional relationships have been proposed for describing the dependency between K, θ and Ψ [38]. From this point on, the *van Genuchten-Mualem* parameterisation is applied. It is given by

For $\Psi \leq 0$

$$\theta(\Psi) = \theta_R + (\theta_S - \theta_R)\left[\frac{1}{1 + (-\alpha\Psi)^n}\right]^{\frac{n-1}{n}}, \tag{2.42}$$

$$\begin{aligned} K(\theta(\Psi)) &= K_S\theta(\Psi)^{\frac{1}{2}}\left[1 - \left(1 - \theta(\Psi)^{\frac{n}{n-1}}\right)^{\frac{n-1}{n}}\right]^2 \\ &= K_S\frac{\left[1 - (-\alpha\Psi)^{n-1}\left[1 + (-\alpha\Psi)^n\right]^{\frac{1-n}{n}}\right]^2}{\left[1 + (-\alpha\Psi)^n\right]^{\frac{n-1}{2n}}}. \end{aligned} \tag{2.43}$$

For $\Psi > 0$

$$\theta = \theta_S, \tag{2.44}$$

$$K = K_S. \tag{2.45}$$

Here, θ_R is the residual water content, θ_S the saturated water content, K_S is the saturated hydraulic conductivity and α and n are van Genuchten curve fitting parameters [10]. θ_R, θ_S, α, n, K_S are material specific constants. Equations (2.42)

and (2.43) are valid for the unsaturated soil zone, while eqs. (2.44) and (2.45) holds for the saturated zone.

In this thesis the focus is on the strictly unsaturated flow regime, i.e. $\Psi < 0$, $\theta' > 0$ and $K > 0$. From [38], it is worth noting that in the present setting the Richards equation degenerates whenever $\Psi \to -\infty$, implying that both $\theta'(\Psi)$ and $K(\theta(\Psi))$ are approaching 0, or situated in the fully saturated regime ($\Psi \geq 0$), when $\theta'(\Psi) = 0$. The regions of degeneracy depend on the saturation of the medium; therefore these regions are not known *a priori* and may vary in space and time.

2.3 Non-Standard Models

The model derived in section 2.2 is based on the validity of eq. (2.34) (and eq. (2.39)). This includes an equilibrium assumption, which is not necessarily true. There is experimental evidence (Hassanizadeh et al. [18, 39]) that dynamic effects and hysteresis are playing an important role and therefore eq. (2.34) is not valid in this form. These effects also have the potential of describing phenomena such as saturation overshooting or finger formation, see D.A.Dicarlo [9], which is not the case for Richards' equation based on the static relation eq. (2.34).

In the following some mathematical models which include non-equilibrium effects and/or hysteretic effects will be presented. Such models are referred to as non-standard models.

2.3.1 Dynamic Capillary Pressure and Hysteresis

To present the principle of hysteresis, an experiment from [2] p. 77-79 will be reproduced. Assuming a sample of porous medium with pores filled with the wetting fluid, see Figure 2.3. There is a left reservoir of wetting fluid and a right reservoir with nonwetting fluid. Further assuming that the pressure in the two reservoirs are controllable, the top and bottom of the sample are impermeable and the influence of gravity can be neglected.

By increasing the pressure in the nonwetting fluid, it is possible to measure the amount of wetting fluid displaced. When equilibrium is reached, a data point relating the capillary pressure and the saturation is produced. The experiment can be repeated with varying pressure differences to collect several data points. Plotting these data points will give a typical capillary pressure - saturation curve, see Figure 2.4.

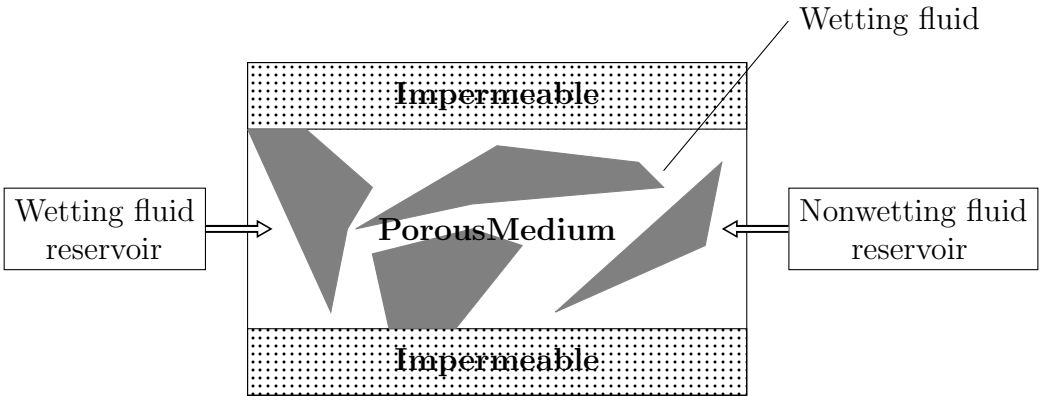

FIGURE 2.3: Sample of porous medium with left reservoir filled with wetting fluid and right reservoir filled with nonwetting fluid.

From this, four points can be made. First, the process where nonwetting fluid displaces wetting fluid is referred to as *drainage*, while when wetting fluid displaces nonwetting it is called *imbibition*. Second, the residual saturation values (S_α^{res}) are clearly represented, which in this case means that the soil is never completely dry. Thirdly, there is an obvious difference between the curves for drainage and imbibition, meaning that the relation between the capillary pressure and the saturation depends on the history. Therefore, it is not enough to know the saturation at one point to determine the capillary pressure, but it is also important to know if the saturation is increasing (imbibition) or decreasing (drainage). Such behaviour is called *hysteresis*, or the process is said to be *hysteretic*. The *primary drainage* curve includes full saturation ($S_w = 1$) as one of its end points, relating to no nonwetting fluid to start with. *Main drainage* and *main imbibition* curves are curves that begin at the residual saturation points of the other fluid. Lastly, the curves that begin at points between the two residual saturations are referred to as *scanning curves*. The fourth point is that a finite capillary pressure is required before any drainage displacement begins. The capillary pressure required to initiate displacement of the wetting fluid is called the *entry pressure*. *Capillary exclusion* is the phenomenon whereby nonwetting fluid is unable to enter particular spatial regions that are filled with wetting fluid due to failure to reach this entry pressure.

Thus an important feature of the macroscopic capillary pressure-saturation curve is its hysteretic behaviour observed when reversing the flow direction, e.g. from drainage to imbibition [16]. The standard relationship assumed between capillary pressure and saturation, see eq. (2.38), is empirical in nature, and as such lacks a firm theoretical foundation [39]. In fact, the relationship $p_n - p_\omega = p_c$ is valid only under static condition. Under dynamic conditions, $p_n - p_\omega$ depends on the

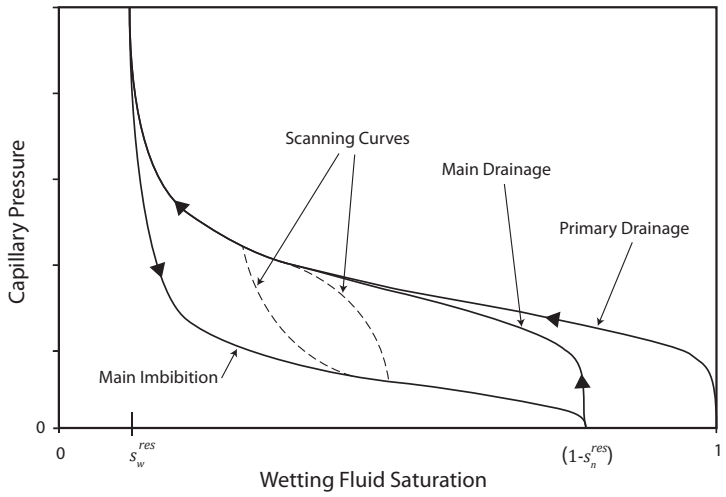

FIGURE 2.4: Typical form for a capillary pressure-saturation curve. *From Nordbotten et al. [2].*

flow velocity, which at larger time scales manifest itself as a change in saturation with time [16].

Hassanizadeh and Gray (1990) [18] suggested that the hysteretic behaviour of the capillary pressure is related to the configuration of interfaces, since fluid pressures vary spatially within each flowing phase, macroscale (or average) pressure values will be different from pressure values at the interface [16]. Based on thermodynamic considerations, they concluded that the hysteretic behaviour of the capillary pressure-saturation relationship can be modelled by including the specific interfacial area in the formulation [16]. In other words, they advocated a dynamic capillary pressure, where the capillary pressure depends not only on the saturation and saturation direction but also the rate of saturation change [9]. For the remainder of this thesis, the focus will be on the effects of including dynamic capillary pressure in the model, while the effects of hysteresis are left unexplored.

2.3.2 Extension of the Standard Model

In order to include non-equilibrium effects in the model, an extension will be added to the Richards' equation. Most continuum models that are proposed are extensions of Richards' equation as derivation of this only requires the Darcy law and conservation of mass, in addition to the fact that the Richards equation works in almost all cases [9]. The extension is related to the concept of dynamic capillary pressure and yields additional terms of the $\theta - \Psi$ relationship. In the

literature there are several different extension models available, a collection of which is presented in [16], p. 10-11. For the further study of these phenomena in this thesis, an equation based on thermodynamic considerations suggested by *Hassanizadeh and Gray* (1990) [18] and *Kalaydjian* (1992) [17] is applied [16]. The equation relates the difference in the phase pressure $p_a - p_w$ to a capillary pressure p_c by

$$p_a - p_w = p_c(\theta_w) - \tau(\theta_w)\frac{\partial \theta_w}{\partial t}. \tag{2.46}$$

Here, $\tau(\theta_w) \geq 0$ is a non-equilibrium coefficient. In this formulation, p_c is an intrinsic property of the porous medium-fluids system, whereas the fluid pressure difference $p_a - p_w$ is dependent on flow dynamics (and thus initial and boundary conditions) [16]. The pressure difference between the air and water phase is equal to a capillary pressure only under static condition. Equation (2.46) suggests that at any given point in time where equilibrium is disturbed, the saturation will change to reestablish the equilibrium condition, and the coefficient $\tau(\theta_w)$ controls this process [16].

Recall from section 2.2.3, that since the pressure of the air phase is assumed equal to the atmospheric pressure everywhere, there is no need to solve for p_a. Also utilising that p_w can be set to be equal to the pressure head Ψ_w, eq. (2.46) takes the form

$$\Psi_w = -p_c(\theta_w) + \tau(\theta_w)\frac{\partial \theta_w}{\partial t}, \tag{2.47}$$

with p_c being the equilibrium (or static) capillary pressure.

The time derivative of θ_w in the Richards' equation (eq. (2.41)) is replaced by the rearrangement of eq. (2.47), given by

$$\frac{\partial \theta_w}{\partial t} = \frac{1}{\tau(\theta_w)}\Psi_w + \frac{1}{\tau(\theta_w)}p_c(\theta_w). \tag{2.48}$$

The static capillary pressure $p_c(\theta_w)$ is given by the *van Genuchten-Mualem* parameterisation

$$p_c(\theta_w) = \frac{\left[\left(\frac{\theta_w - \theta_R}{\theta_S - \theta_R}\right)^{-\frac{n-1}{n}} - 1\right]^{\frac{1}{n}}}{\alpha}. \tag{2.49}$$

Equation (2.49) is obtained by inverting the relation eq. (2.42)

2.4 The Mathematical Model

As a final note to the chapter, a summary of the equations derived in the previous sections is presented. Thus establishing the representative mathematical models used to describe porous media flow. The models will found the basis for the numerical analysis developed in chapter 3.

2.4.1 Simplifications of the Mathematical Model

The following assumptions are set to hold true for all problems considered in subsequent chapters:

- the density ρ is constant,
- the porosity ϕ is constant,
- the temperature T is constant,
- dissolved components do *not* influence the flow.

The first assumption is utilised in section 2.2.3, eq. (2.35), to yield the described Richards' equation (eq. (2.41)). From assuming the temperature and porosity to be constant the fluids are said to be *incompressible*, see section 2.1.2. The final assumption is necessary to ensure that no additional relations or equations are needed to describe the flow of water containing dissolved components.

2.4.2 Representative Equations

Summing up the equations for the flow in a porous medium introduced in sections 2.1 to 2.3, yields the following mathematical models.

Standard Models

The Richards equation without any additional relations or extensions, as well as the convection-diffusion equation are defined as the standard models. Assuming

all equations models flow for the water phase, the subscript w is omitted for the remainder of the thesis, and the model for the Richards' equation becomes

$$\begin{cases} \partial_t \theta(\Psi) - \nabla \cdot [K(\Psi)\nabla(\Psi + z)] = f, & \text{in } \Omega, \\ \theta(\Psi), \;\; K(\Psi), & \text{in } \Omega, \\ \Psi(t,x)|_{t=0} = \Psi_0(x), & \text{in } \Omega, \\ \Psi(t,x) = \Psi_D \;\; \text{or} \;\; \mathbf{n}^T \mathbf{K} \nabla(\Psi + z) = q_{N_1}, & \text{on } \partial\Omega, \end{cases} \tag{2.50}$$

with $\theta(\Psi)$ and $K(\Psi)$ given by the van Genuchten-Mualem parameterisation in section 2.2.4. Initial and boundary conditions are needed to ensure uniqueness of the solution, given by $\Psi_0(x)$ and Ψ_D, q_{N_1} respectively. Here Ψ_D represents Dirichlet boundary conditions and q_{N_1} are Neumann boundary conditions (see section 3.2.3). Ω is a domain in space consisting of a porous medium with $\partial\Omega$ as its boundary.

The model for the convection-diffusion equation becomes

$$\begin{cases} \partial_t(\theta c) - \nabla \cdot (\theta D \nabla c - \mathbf{u}c) = Q, & \text{in } \Omega, \\ \mathbf{u} = -K(\Psi)\nabla(\Psi + z), & \text{in } \Omega, \\ c(t,x)|_{t=0} = c_0(x), & \text{in } \Omega, \\ c(t,x) = c_D \;\; \text{or} \;\; \mathbf{n}^T(\theta D \nabla c - \mathbf{u}c) = q_{N_2}, & \text{on } \partial\Omega. \end{cases} \tag{2.51}$$

The convection-diffusion equation is coupled with the Richards equation, so that the volumetric flux, $\mathbf{u}$, originally resulting from the Darcy law (eq. (2.40)), and the water content θ are obtained from the computations of Richards' equation. As in the case of the model for the Richards equation, initial and boundary conditions are included to ensure uniqueness of the solution, where c_D and q_{N_2} are Dirichlet and Neumann conditions respectively.

Non-Standard Model

The non-standard model is given by the Richards equation with the extension for the dynamic capillary pressure, defined in section 2.3.2, included. The model becomes

$$\begin{cases} \partial_t \theta - \nabla \cdot [K(\theta)\nabla(\Psi + z)] = f, & \text{in } \Omega, \\ \Psi = -p_c(\theta) + \tau(\theta)\partial_t \theta(\Psi), & \text{in } \Omega, \\ K(\theta), \;\; p_c(\theta), \;\; \tau(\theta) & \text{in } \Omega, \\ \Psi(t,x)|_{t=0} = \Psi_0(x), & \text{in } \Omega, \\ \Psi(t,x) = \Psi_D \;\; \text{or} \;\; \mathbf{n}^T \mathbf{K} \nabla(\Psi + z) = q_{N_1}, & \text{on } \partial\Omega. \end{cases} \tag{2.52}$$

In this, the time derivative in Richards' equation is replaced by the expression given by the second equation, resulting in a *pseudo-parabolic equation*, where dynamic effects are included in the capillary pressure [22]. The capillary pressure $p_c(\theta)$ is described in eq. (2.49), and $\tau(\theta)$ is given by some function. $K(\theta)$ is given by the first relation in eq. (2.43), and the initial and boundary conditions will be defined in the same manner as in the standard model, (2.50). The Convection-Diffusion equation, given by (2.51), is also coupled with this model. The case when $\tau = 0$ corresponds to the standard model.

Chapter 3

Numerical Methods

In the previous chapter, a coupled set of partial differential equations was obtained. These sets of equations will be solved numerically in one spatial dimension (1D), using finite difference methods and a finite volume method known as the two-point flux approximation scheme or simply TPFA [12]. This chapter will present the theoretical background for the discretisation of the equations, also including the fully discretised schemes in space and time. The Richards equation and the equation giving the non-standard extension are both nonlinear, and thus need to be linearised in order to be solved numerically. In section 3.4 robust linearisation schemes are presented for Richards' equation with and without dynamic capillary pressure. The scheme for the Richards equation with dynamic capillarity is new, whereas the one for the standard Richards' equation is the one in [37, 40] but for a TPFA discretisation. The schemes will be shown to be robust and linearly convergent, in addition to have certain advantages compared to the more widespread and commonly used linearisation methods. Lastly, a short comment about the implementation of the numerical schemes is made.

3.1 Grid

One of the first steps of implementing methods for solving a mathematical problem numerically, requires a 'geometric discretisation' of the domain Ω [5]. The discretisation is often constructed by placing grid points throughout the domain and connecting these points using nonintersecting, straight lines [19]. In two dimensions (2D) the grid points now make up the corners of the grid cells.

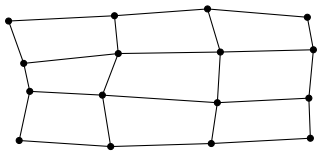

FIGURE 3.1: Point-distributed grid

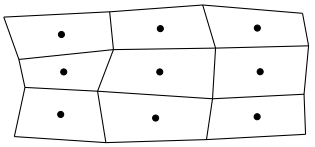

FIGURE 3.2: Cell-centered grid

For a function $f(\mathbf{x})$ defined on the domain of the grid, the grid points are used to provide a discretised representation of the function. Let $\mathbf{x}_i$, $i = 1, 2, ..., N$ denote the grid points of a grid. A discretised representation of f is then given by

$$\boldsymbol{f} = [f(\mathbf{x}_1), ..., f(\mathbf{x}_N)]^T. \tag{3.1}$$

There are in principle two main types of grids, when applied results in different discretised representations of the function f. These are point-distributed grids and cell-centred grids. When the grid points are placed at the corners of the cells it is known as a point-distributed grid, while a cell-centred grid has its grid points in the centres of the cell [19], see Figures 3.1 and 3.2. For a cell-centred grid the grid must be generated before the cell-centred points can be determined, even for one-dimensional grids. In general, it is not possible to place a random set of points throughout the domain, before creating a grid around the points, so that they make up the cell-centres [19].

The TPFA scheme is a cell-centred finite-volume method [12]. Thus, the one-dimensional interval in space is discretised using a cell-centred grid. The spacing is assumed to be equidistant. First, the interval $[0, L]$ is divided into N equal cells. The walls of the cells are given by $x_{i+\frac{1}{2}} = ih$ for $i = 1, 2, \ldots, N$, where $h = x_{i+\frac{1}{2}} - x_{i-\frac{1}{2}} = L/N$. Then $x_{\frac{1}{2}} = 0$ and $x_{N+\frac{1}{2}} = L$ denotes the boundaries of the domain, see Figure 3.3.

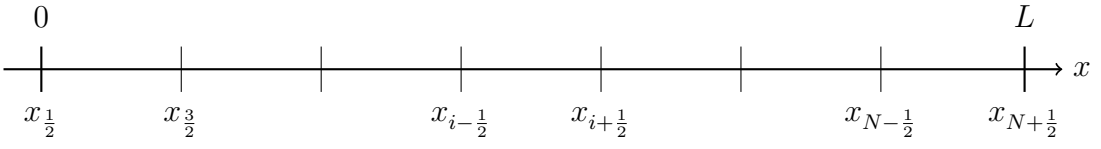

FIGURE 3.3: Space interval divided into N equidistant cells.

After the space interval is divided into equidistant cells, the cell-centred points are defined and denoted by the grid points $x_1, x_2, \ldots, x_N$, see Figure 3.4. Since the grid is equidistant, the distance between neighbouring grid points equals the

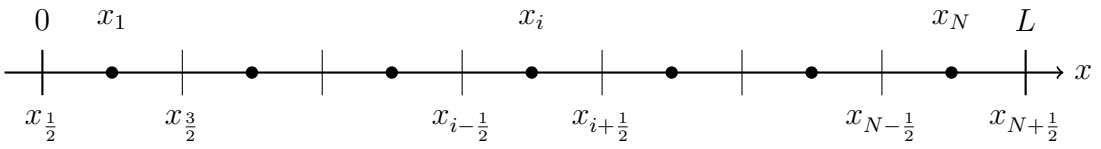

FIGURE 3.4: Cell-centred discretisation in space.

length of each cell, $\Delta x = x_{i+1} - x_i = h$. Then $x_1 = h/2$ and $x_i = ih - h/2$ for $i = 0, \ldots, N$. The rightmost grid point is $x_N = Nh - h/2 = L - h/2$.

Equivalently to the discretisation in space, there is also a discretisation in time, see Figure 3.5. The time interval $[0, T]$, spans from initial time, $t_0 = 0$, to final time, $t_m = T$. As in the case with the spatial grid points, the time steps are assumed equidistant, given by $\Delta t = t_{j+1} - t_j = T/m$, for $j = 0, 1, \ldots, m$.

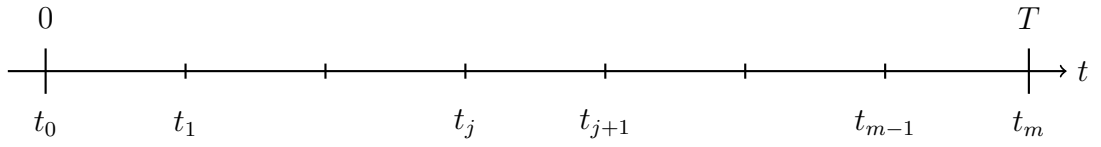

FIGURE 3.5: Equidistant time discretisation.

3.2 Discretisation in Space

In order to solve a PDE by the means of a numerical method, the equation must be discretised. The PDEs in the mathematical models from section 2.4.2 are dependent on space and time, and thus need to be discretised with respect to both variables. The main focus in this section will however be on the discretisation in space and on boundary conditions. There are several ways to perform spatial discretisation of a PDE. The method chosen in this thesis is, as mentioned previously the TPFA scheme, which is recognised as a *control volume method* (CVM) also referred to as a *finite-volume method* [12, 19]. CVMs are a class of numerical methods used to apply spatial discretisation to PDEs. They are popular methods due to the fact that they satisfy the physical principle of mass conservation, in addition to being fairly easy to formulate for complex grids. For 1D, the TPFA is equivalent to the finite difference method for a cell-centred grid.

3.2.1 Finite Difference Method

One of many different approaches to solving PDEs numerically, are finite difference methods. It is an elementary discretisation method, in which the derivatives in a differential equation are replaced by finite difference approximations at a discrete set of points in space or time. The resulting set of equations, can then be solved by algebraic methods [20]. For further study of the finite difference method, besides what will be presented in the following, see [8, 19, 20, 21].

To establish appropriate finite difference approximations of derivatives, Taylor series are applied. Recall from calculus [6], that for $f(x \pm h) = f(x_{i\pm1})$,

$$f(x_{i\pm1}) = f(x) \pm f'(x_i)h + f''(x_i)\frac{h^2}{2!} \pm f'''(x_i)\frac{h^3}{3!} + \dots \tag{3.2}$$

Using the + series, the *forward* difference approximation for the first derivative is attained

$$f'(x_i) = \frac{f(x_{i+1}) - f(x_i)}{h} + O(h), \tag{3.3}$$

while the − series results in the *backward* difference approximation for the first derivative

$$f'(x_i) = \frac{f(x_i) - f(x_{i-1})}{h} + O(h). \tag{3.4}$$

These approximations are first order accurate, given by the term $O(h)$, also referred to as the *truncation error*. To attain a better approximation, the negative sign in eq. (3.2) can be subtracted from the positive sign, to get the *centred* difference approximation

$$f'(x_i) = \frac{f(x_{i+1}) - f(x_{i-1})}{2h} + O(h^2). \tag{3.5}$$

This approximation is second order accurate ($O(h^2)$).

For the second order derivative, a centred finite difference approximation is achieved by adding the two series in eq. (3.2), to give

$$f''(x_i) = \frac{f(x_{i+1}) - 2f(x_i) + f(x_{i-1})}{h^2} + O(h^2). \tag{3.6}$$

As with the centred difference, this approximation yields a truncation error of order h^2, meaning they are more accurate approximations than eqs. (3.3) and (3.4). This is as expected from geometric considerations.

By applying eq. (3.6) to the ordinary differential equation (ODE)

$$-(Ku_x)_x = f, \tag{3.7}$$

with K constant, the approximation for the second derivative becomes

$$-Ku_{xx} \approx K\frac{-u(x_{i+1}) + 2u(x_i) - u(x_{i-1})}{h^2}. \tag{3.8}$$

This can be expressed by the linear system matrix system

$$\boldsymbol{Au} = \boldsymbol{b}, \tag{3.9}$$

where

$$\boldsymbol{A} = \frac{K}{h^2}\begin{bmatrix} 2 & -1 & & & \\ -1 & 2 & -1 & & \\ & \ddots & \ddots & \ddots & \\ & & -1 & 2 & -1 \\ & & & -1 & 2 \end{bmatrix}, \tag{3.10}$$

and

$$\boldsymbol{b} = \begin{bmatrix} f(x_0) \\ f(x_1) \\ \vdots \\ f(x_N) \\ f(x_{N+1}) \end{bmatrix}, \tag{3.11}$$

for $i = 1, \ldots, N$.

3.2.2 Two-Point Flux Approximation

Unlike finite difference methods where partial derivatives are replaced by divided differences, see section 3.2.1, finite volume methods have a more physical motivation and are derived from conservation of (physical) quantities over cell volumes [12]. One finite volume method is the TPFA scheme, which is undoubtedly one of the simplest discretisation techniques for elliptic equations. However, it is still widely used for simulation purposes due to its simplicity and the method yielding explicit expressions for the fluxes and harmonic averaging of the permeability, see [19]. It holds when the flux is equal on both sides of the cell wall. The theory

described in this section is based on the lecture notes by I.Aavatsmark [19] and obtained through personal communication with F.A.Radu [13] while he was lecturing the course *Flow in Porous Media* (MAT254).

As in section 3.2.1, an ordinary differential equation (ODE) is given by

$$-(Ku_x)_x = f, \tag{3.12}$$

where $K = K(x)$ denotes the permeability and f some source-term. The index denotes the derivative with respect to x. The TPFA is based on the integral formulation of the problem given by

$$\int_{\partial\Omega_i} q \cdot \boldsymbol{n}\, dS = \int_{\Omega_i} f\, dx. \tag{3.13}$$

Applying the divergence theorem [6] generates the left hand side of eq. (3.13), with $\boldsymbol{q} = -Ku_x$. The domain of the ODE is discretised by a cell-centred, one-dimensional grid, see Figure 3.6. The grid points denoted by x_i for $i = 0, \ldots, N$ are thus located at the centres of the cells, and the cell walls are given by $x_{i-\frac{1}{2}}$ and $x_{i+\frac{1}{2}}$.

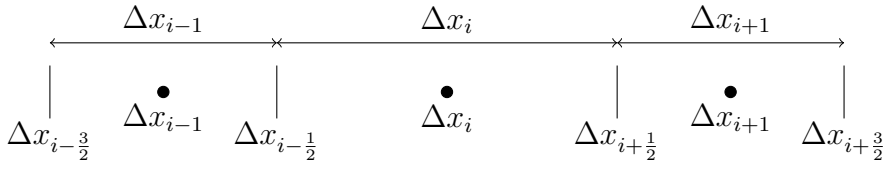

FIGURE 3.6: Cell-centred grid with grid points x_i and cell walls $x_{i+\frac{1}{2}}$.

Integrating eq. (3.13) over the i^{th} cell, from $x_{i-\frac{1}{2}}$ to $x_{i+\frac{1}{2}}$, gives

$$q_{i+\frac{1}{2}} - q_{i-\frac{1}{2}} = \int_{x_{i-\frac{1}{2}}}^{x_{i+\frac{1}{2}}} f(x)dx. \tag{3.14}$$

To obtain an expression for $q_{i+\frac{1}{2}}$ as a function of u, it first requires a rewriting of the relation $q = -Ku_x$ to get

$$u_x = -\frac{q}{K(x)}. \tag{3.15}$$

By integrating eq. (3.15) from x_i to x_{i+1}, the relation,

$$u_{i+1} - u_i = -q_{i+\frac{1}{2}} \int_{x_i}^{x_{i+1}} \frac{1}{K(x)}\, dx, \tag{3.16}$$

is obtained. This relation can be manipulated to give the desired expression for $q_{i+\frac{1}{2}}$, given by

$$q_{i+\frac{1}{2}} = -\frac{u_{i+1} - u_i}{\int_{x_i}^{x_{i+1}} \frac{1}{K(x)}\, dx}. \tag{3.17}$$

It now remains to derive an expression for the integral

$$\int_{x_i}^{x_{i+1}} \frac{1}{K(x)}\, dx. \tag{3.18}$$

For a cell-centred grid, $K(x)$ is assumed constant on each cell, denoted by the values at the grid points so that $K_i = K(x_i)$. From Figure 3.6, $\Delta x_i = x_{i+\frac{1}{2}} - x_{i-\frac{1}{2}}$, represents the distance between the walls of the cell. Since x_i and x_{i+1} are grid points of two neighbouring cells, the integral is approximated by taking the average over the two cells involved, given by

$$\int_{x_i}^{x_{i+1}} \frac{1}{K(x)}\, dx = \frac{1}{2}\left(\frac{\Delta x_{i+1}}{K_{i+1}} + \frac{\Delta x_i}{K_i}\right). \tag{3.19}$$

The approximation in eq. (3.19) holds for *non-equidistant*, cell-centred grids. In this thesis however, *equidistant*, cell-centred grids with $\Delta x_i = h$ are considered, which leads to the expression

$$\int_{x_i}^{x_{i+1}} \frac{1}{K(x)}\, dx = \frac{h}{2}\left(\frac{1}{K_{i+1}} + \frac{1}{K_i}\right). \tag{3.20}$$

Inserting eq. (3.20) into eq. (3.17) gives

$$q_{i+\frac{1}{2}} = -\frac{u_{i+1} - u_i}{\frac{h}{2}\left(\frac{1}{K_{i+1}} + \frac{1}{K_i}\right)}. \tag{3.21}$$

Finally, by inserting the equations for q for an equidistant, cell-centred grid, eq. (3.14) becomes

$$\frac{u_i - u_{i-1}}{\frac{h}{2}\left(\frac{1}{K_i} + \frac{1}{K_{i-1}}\right)} - \frac{u_{i+1} - u_i}{\frac{h}{2}\left(\frac{1}{K_{i+1}} + \frac{1}{K_i}\right)} = \int_{x_{i-\frac{1}{2}}}^{x_{i+\frac{1}{2}}} f(x)dx. \tag{3.22}$$

Equation (3.22) can be expressed as

$$a_i(u_i - u_{i-1}) - a_{i+1}(u_{i+1} - u_i) = b_i, \tag{3.23}$$

by denoting

$$a_i = \frac{1}{\frac{h}{2}\left(\frac{1}{K_i} + \frac{1}{K_{i-1}}\right)}, \tag{3.24}$$

$$b_i = \int_{x_{i-\frac{1}{2}}}^{x_{i+\frac{1}{2}}} f(x)dx \approx hf_i, \tag{3.25}$$

where f_i is defined as

$$f_i = \frac{1}{h}\int_{x_{i-\frac{1}{2}}}^{x_{i+\frac{1}{2}}} f(x)dx, \tag{3.26}$$

and the second relation in eq. (3.25) arise from applying the midpoint rule [24].

Rearranging eq. (3.23) leads to the system of equations

$$-a_i u_{i-1} + (a_i + a_{i+1})u_i - a_{i+1}u_{i+1} = b_i, \tag{3.27}$$

for $i = 1, \ldots, n$. Hence, being a system of n equations. The unknowns u_i can be collected in the vector $\boldsymbol{u} = [u_0, \ldots, u_{n+1}]^T$. That is, there are $n + 2$ unknowns in n equations. In order to achieve a unique solution, additional boundary conditions are needed and will be considered in the following section, see section 3.2.3. The system of equations in eq. (3.27) can be represented by the following matrix representation

$$\boldsymbol{Au} = \boldsymbol{b}, \tag{3.28}$$

where the sparse, tridiagonal coefficient matrix A is given by

$$\boldsymbol{A} = \begin{bmatrix} -a_1 & a_1 + a_2 & -a_2 & & & & \\ & -a_2 & a_2 + a_3 & -a_3 & & 0 & \\ & & \ddots & \ddots & \ddots & & \\ & & & -a_{n-1} & a_{n-1} + a_n & -a_n & \\ & 0 & & & -a_n & a_n + a_{n+1} & -a_{n+1} \end{bmatrix} \tag{3.29}$$

As a final mark, it is worth noting that the TPFA scheme only yields consistent flux approximations for $\boldsymbol{K}$-orthogonal grids [14, 23]. A grid is said to be $\boldsymbol{K}$-orthogonal if and only if the flux across all edges can be approximated to a two-point flux in a consistent way [19]. For further reading on the properties of $\boldsymbol{K}$-orthogonal grids see [19] p. 144-146.

3.2.3 Boundary Conditions

PDEs has to be supplemented by initial and boundary conditions in order to specify a particular situation where a unique solution is expected, see section 2.4.2. Boundary conditions are specifications on the boundary of the domain, $\partial\Omega$ [5]. For a one-dimensional domain, or interval, the boundary consists of two separate boundary points located at the left and right side of the interval, see Figure 3.4. Two of the principle types of boundary conditions will be presented in the following, these are Dirichlet and Neumann boundary conditions. Depending on the problem, it can in some cases be convenient to apply the same boundary condition at the left and right boundary, while in others a combination of boundary conditions are more fitting.

Dirichlet Boundary Conditions

For a system of PDEs, the Dirichlet boundary condition is given by the function value of the unknown at the boundaries of the domain. To provide an outline of Dirichlet boundary conditions, the stationary, one-dimensional problem eq. (3.12), where $u = u(x)$ is the unknown, will be considered on the domain $[0, L]$. The Dirichlet boundary conditions are then given by

$$u(0) = u_0, \tag{3.30}$$

and

$$u(L) = u_L. \tag{3.31}$$

Since the grid applied in the discretisation of the domain is assumed to be cell-centred, Figure 3.4, the discretised form of the boundary conditions become

$$u_{\frac{1}{2}} = u_0, \tag{3.32}$$

and

$$u_{n+\frac{1}{2}} = u_L, \tag{3.33}$$

For a point-distributed grid, the boundary points will coincide with the grid points at the left- and rightmost endpoints, making the construction of Dirichlet boundary conditions straight forward, as u is defined at the grid points. This is not the case however for cell-centred grids, as is evident from eqs. (3.32) and (3.33). Alternative methods for handling the boundary conditions are thus needed. In

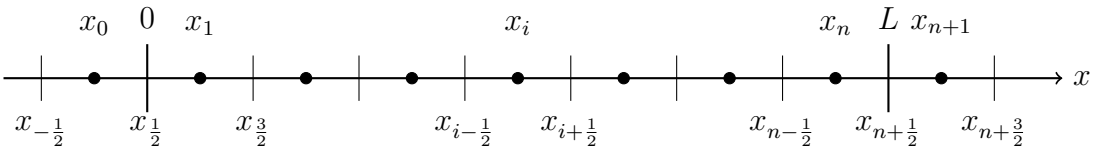

FIGURE 3.7: Cell-centred grid with ghost cells included at the boundaries of the interval.

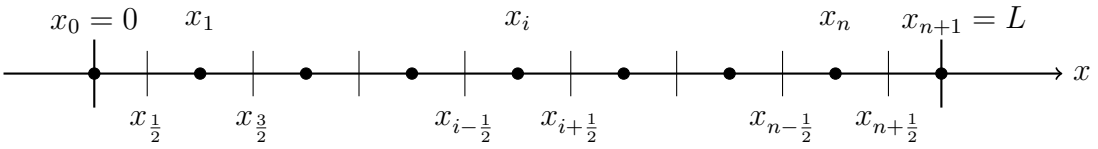

FIGURE 3.8: Cell-centred grid with adjusted half cells near the boundaries of the interval.

[21], two ways to construct Dirichlet boundary conditions for cell-centred grids are presented.

The first method consists of including a ghost cell at each boundary as shown in Figure 3.7. It is then assumed that the Dirichlet boundary condition is prescribed at the centre of the ghost cell and the usual approach is followed to derive the difference equation on the first and last cell. Two additional grid points, x_0 and x_{n+1}, are thus created, and the Dirichlet boundary conditions can be defined as

$$u_0 = u_0, \tag{3.34}$$

and

$$u_{n+1} = u_L. \tag{3.35}$$

It is noted in [21] that prescribing the Dirichlet boundary condition at the centre of the ghost cell instead of the boundary is a first order approximation, and will not be adequate if the solution is strongly dependent on the distance away from the boundary condition. The second method is to include a half cell at the endpoints of the interval as done in Figure 3.8. In this case, no equation is derived on the 1^{st} cell, but rather derived on the 2^{nd} cell and when it reaches the 1^{st} cell it takes on the Dirichlet boundary condition [21].

When applying the method of adding ghost cells to the ends of an interval discretised using a cell-centred grid, the Dirichlet boundary condition is more or less handled the same way as for a point-distributed or vertex centred grid. The difference is where the grid points, x_i, are defined and consequently in what points

u is computed. This can be demonstrated by using the discretisation of eq. (3.12) given by eq. (3.27) in section 3.2.2. Thus, the system of equations looks like

$$\begin{aligned}
-a_1u_0 + (a_1 + a_2)u_1 - a_2u_2 &= b_1 \\
-a_2u_1 + (a_2 + a_3)u_2 - a_3u_3 &= b_2 \\
&\vdots \\
-a_{n-1}u_{n-2} + (a_{n-1} + a_n)u_{n-1} - a_nu_n &= b_{n-1} \\
-a_nu_{n-1} + (a_n + a_{n+1})u_n - a_{n+1}u_{n+1} &= b_n
\end{aligned}$$

The Dirichlet boundary conditions are given by $u_0 = u_0$ and $u_{n+1} = u_L$ (eqs. (3.34) and (3.35)), and the terms involving the boundary conditions can be moved to the right hand side of the system, giving

$$\begin{aligned}
(a_1 + a_2)u_1 - a_2u_2 &= b_1 + a_1u_0 \\
-a_2u_1 + (a_2 + a_3)u_2 - a_3u_3 &= b_2 \\
&\vdots \\
-a_{n-1}u_{n-2} + (a_{n-1} + a_n)u_{n-1} - a_nu_n &= b_{n-1} \\
-a_nu_{n-1} + (a_n + a_{n+1})u_n &= b_n + a_{n+1}u_L
\end{aligned}$$

This can be expressed as the system

$$\boldsymbol{Au} = \boldsymbol{b}, \tag{3.36}$$

for $\boldsymbol{u} = [u_1, \ldots, u_n]^T$, where

$$\boldsymbol{A} = \begin{bmatrix}
a_1 + a_2 & -a_2 & & & & \\
-a_2 & a_2 + a_3 & -a_3 & & \mathbf{0} & \\
& \ddots & \ddots & \ddots & & \\
& & -a_{n-1} & a_{n-1} + a_n & -a_n & \\
\mathbf{0} & & & -a_n & a_n + a_{n+1}
\end{bmatrix} \tag{3.37}$$

and

$$\boldsymbol{b} = \begin{bmatrix}
b_1 + a_1u_0 \\
b_2 \\
\vdots \\
b_{n-1} \\
b_n + a_{n+1}u_L
\end{bmatrix}. \tag{3.38}$$

Neumann Boundary Conditions

For the case when Neumann boundary conditions are imposed, the values that the derivative of the function is to take on the boundary are specified. That is, the Neumann boundary conditions for a one-dimensional domain is given by

$$-Ku_x(0) = u_\alpha, \tag{3.39}$$

and

$$-Ku_x(L) = u_\beta \tag{3.40}$$

Recalling that $x_{\frac{1}{2}} = 0$ and $x_{n+\frac{1}{2}} = L$, see Figure 3.4. Again, demonstrating by the discretisation of eq. (3.12), and using the fact that the flux q is given by $q = -K_i(x)u_x$, the derivative at the cell wall, $x_{i+\frac{1}{2}}$, is expressed by $q_{i+\frac{1}{2}}$. Thus, the boundary conditions are given by

$$q_{\frac{1}{2}} = u_\alpha, \tag{3.41}$$

and

$$q_{n+\frac{1}{2}} = u_\beta. \tag{3.42}$$

From eqs. (3.14) and (3.25),

$$q_{i+\frac{1}{2}} - q_{i-\frac{1}{2}} = b_i, \tag{3.43}$$

for $i = 1, \ldots, n$. The first equation, when $i = 1$, becomes

$$q_{\frac{3}{2}} - q_{\frac{1}{2}} = b_1, \tag{3.44}$$

where $q_{\frac{1}{2}} = u_\alpha$ is given by the boundary condition, eq. (3.41), and eq. (3.44) can be expressed as

$$q_{\frac{3}{2}} = b_1 + u_\alpha. \tag{3.45}$$

Similarly for the last equation, when $i = n$, eq. (3.41) becomes

$$q_{n-\frac{1}{2}} = b_n + u_\beta. \tag{3.46}$$

From observation of the above equations, it is worth noting that when discretising a system of equations using a cell-centred grid like the one in Figure 3.4, Neumann boundary conditions are the natural choice. This is due to the flux boundary condition being located at the boundary, making considerations of ghost cells or half-cells unnecessary.

Lastly, recalling eqs. (3.21) and (3.24), where

$$q_{i+\frac{1}{2}} = -a_{i+1}(u_{i+1} - u_i), \tag{3.47}$$

the first and last equation become

$$a_2 u_1 - a_2 u_2 = b_1 + u_\alpha \tag{3.48}$$

$$-a_n u_{n-1} + a_n u_n = b_n + u_\beta, \tag{3.49}$$

while the other equations remain unchanged. As in the case with Dirichlet boundary conditions, the set of equations can be displayed with the matrix representation

$$\boldsymbol{Au} = \boldsymbol{b}, \tag{3.50}$$

where

$$\boldsymbol{A} = \begin{bmatrix} a_2 & -a_2 & & & & \\ -a_2 & a_2 + a_3 & -a_3 & & \mathbf{0} & \\ & \ddots & \ddots & \ddots & & \\ & & & -a_{n-1} & a_{n-1} + a_n & -a_n \\ \mathbf{0} & & & & -a_n & a_n \end{bmatrix} \tag{3.51}$$

and

$$\boldsymbol{b} = \begin{bmatrix} b_1 + u_\alpha \\ b_2 \\ \vdots \\ b_{n-1} \\ b_n + u_\beta \end{bmatrix} \tag{3.52}$$

for $\boldsymbol{u} = [u_1, \ldots, u_n]^T$.

3.3 Discretisation in Time

To present the time discretisation methods, the ODE

$$u'(t) = F(t, u(t)), \tag{3.53}$$

will be considered. From the forward difference approximation in eq. (3.3), the resulting numerical scheme discretised with respect to time is known as the *forward*

Euler scheme, or the *explicit* Euler's method [25, 26], given by

$$u^{n+1} = u^n + \Delta t F(t^n, u^n). \tag{3.54}$$

If the backwards difference approximation in eq. (3.4) is applied instead, the resulting scheme will now be the *backward* Euler scheme, also known as the *implicit* Euler's method [25, 26],

$$u^{n+1} = u^n + \Delta t F(t^{n+1}, u^{n+1}). \tag{3.55}$$

For both relations, $n = 1, \ldots, T$ denotes the time steps, Δt denotes the uniform length of each time step and u^n represents the numerical approximation of the exact solution u at time $t^n = n\Delta t$.

What separates the two methods is the input of the function F, characterising the method as an implicit or explicit method. In [24] a method is called *explicit* if u^{n+1} can be computed in terms of the previous values u^k, $k \leq n$, while it is said to be *implicit* if u^{n+1} depends implicitly on itself through F.

The Euler methods of eqs. (3.54) and (3.55) are Taylor methods of order one [25], meaning they are both first order methods [26]. The stability conditions of the two methods do however differ [24, 25]. While the backward Euler method satisfies the absolute stability property,

$$|u_n| \longrightarrow 0 \quad \text{as} \quad t_n \longrightarrow +\infty, \tag{3.56}$$

where u is the solution of $u'(t) = \lambda t$ with $\lambda < 0$, for *any* value of Δt. This is not the case for the forward Euler method, where the method is stable only for certain values of Δt. For a more detailed study of the stability conditions of the two methods, see [24] p. 480 or [25] p. 609-610. An implicit method generally requires more work than an explicit one, in particular if F is a nonlinear function with respect to u, in which case a linearisation technique must be applied to solve eq. (3.55), see section 3.4. If F is a linear function of u, the equation is simply rearranged and solved for u^{n+1}.

3.4 Linearisation of Nonlinear Equations

The mathematical models presented in this thesis consist of coupled, nonlinear PDEs. This makes the design and implementation of efficient numerical schemes a challenging task. To discretise the equations in space, a locally conservative

finite volume [19, 28, 29, 30, 31] discretisation, see section 3.2.2, is applied due to its alleviation of several stability issues. Furthermore, a fully implicit temporal discretisation is implemented because of its stability properties for all time-scales, see section 3.3.

The spatial and temporal discretisations thus lead to a large system of nonlinear equations for each time step. Common methods for solving such systems are the fix point method [24], Picard's method [5] or Newton's method [5, 32, 33, 34, 35]. The two former are linearly convergent while the latter is quadratically convergent [27]. Newton's method is a powerful tool when applied to systems arising from discretisation of parabolic equations, but the quadratic convergence does however come at a price of only local convergence in solution space. Two main concerns regarding Newton's method is that the Jacobian matrix of the system needs to be assembled, as well as the fact that the convergence of the algorithm is not guaranteed when the initial guess is not "close enough", which implies a restriction on the time step [27].

To treat the nonlinearities of the PDEs in the mathematical models of section 2.4.2, two linearisation schemes are proposed and analysed. The first scheme applies to the standard Richards equation (see section 2.4.2) and is based on the works of M.Slodicka [37] and Radu et al. [36]. It is in this thesis applied for the TPFA method for the first time. See Radu et al. [27] for a similar scheme for two-phase flow. The second linearisation scheme applies to Richards' equation with dynamic capillarity (see section 2.4.2). It continues the works in [36, 37]. The scheme is new. A similar linearisation method was proposed by Fan et al. [22], with saturation as the primary variable.

The linearisation schemes do not involve the computation of derivatives and are shown to be very robust (see sections 3.4.1 and 3.4.2). Moreover, the convergence of the schemes is independent of the mesh diameter, this being an important advantage when compared to other linearisation methods.

3.4.1 Linearisation Scheme for the Richards Equation

The linearisation scheme for the Richards equation is based on the schemes presented in M.Slodicka [37], Radu et al. [36] and F.A.Radu [40]. See [37] for a Galerkin FE based scheme and [36, 40] for mixed finite element (MFEM). Similarly to the proposed linearisation scheme derived for the finite volume method, multi-point flux approximation (MPFA) [12, 19], in the recently published report by Radu et al. [27], the scheme is in the following applied to the TPFA method.

Throughout this thesis the following assumptions on the data and the solution of the continuous problem are considered.

(A1) $\theta(\cdot)$ is monotone increasing and Lipschitz continuous.

(A2) $p_c(\cdot)$ is monotone decreasing and Lipschitz continuous.

(A3) K is constant, $K > 0$.

(A4) τ is constant, $\tau > 0$.

A fully implicit temporal discretisation of Richards' equation (eq. (3.117)), by the backward Euler method, leads to the nonlinear system

$$\theta^{n+1} + \Delta t \boldsymbol{A}_{n+1} \Psi^{n+1} = \Delta t f^{n+1} + \theta^n, \tag{3.57}$$

where $\theta^n = \theta(\Psi^n), \theta^{n+1} = \theta(\Psi^{n+1})$ with Ψ^n, Ψ^{n+1} piecewise constants on the cells, and $\boldsymbol{A}_{n+1}$ is the system matrix given by

$$\boldsymbol{A}_{n+1} = \frac{K}{h^2} \begin{bmatrix} 2 & -1 & & & & \\ -1 & 2 & -1 & & \mathbf{0} & \\ & \ddots & \ddots & \ddots & & \\ & & -1 & 2 & -1 & \\ \mathbf{0} & & & -1 & 2 & \end{bmatrix}, \tag{3.58}$$

for the 1-dimensional case and K constant. For a detailed explanation of how eq. (3.57) is derived see section 3.5.2.

Instead of applying any of the standard approaches to solving eq. (3.57) the linearisation method from Radu et al. [27, 36], M.Slodicka [37] and F.A.Radu [40] is considered. The linearisation is applied in combination with the TPFA method for the first time. Let

$$L_\Psi = \sup_\Psi \frac{d}{d\Psi} \theta(\Psi). \tag{3.59}$$

In practice, any constant $L_\Psi \geq \sup_\psi \frac{d}{d\psi}\theta(\psi)$ will ensure convergence of the scheme, as it will be shown in Theorem 3.1. Then, iterate $j+1$ is obtained by solving the following system of equations

$$L_\Psi(\Psi^{n+1,j+1} - \Psi^{n+1,j}) + \theta(\Psi^{n+1,j}) + \Delta t \boldsymbol{A}_{n+1} \Psi^{n+1,j+1} = \Delta t f^{n+1} + \theta(\Psi^n), \tag{3.60}$$

where $\Psi^{n+1,0} = \Psi^n$. Note that eq. (3.60) is a linear elliptic system. To evaluate the convergence of the linear system the error at iteration step $j+1$ is introduced

$$e_\Psi^{n+1,j+1} = \Psi^{n+1,j+1} - \Psi^{n+1}. \tag{3.61}$$

In order to show the convergence of the scheme, it will be proven that

$$||e_\Psi^{n+1,j+1}|| \longrightarrow 0 \text{ when } j \longrightarrow \infty, \tag{3.62}$$

where $||\cdot||$ is the notation for the discrete L_2 norm, $||e_\Psi^{n+1,j+1}||^2 := \sum_i m_i |\Psi_i^{n+1,j+1} - \Psi_i^{n+1}|^2$. Here m_i represents the length of each subinterval i of the 1-dimensional domain, $m_i = h$ for an equidistant grid. The discrete L_2 scalar product is defined by $\langle u, v\rangle := \sum_i m_i u_i v_i$.

Theorem 3.1. *Assuming (A1),(A3) and that the time step Δt is sufficiently small, and that the finite volume method satisfies* (3.66)*, the linearisation scheme* (3.60) *is (at least) linearly convergent.*

Proof. Subtracting eq. (3.57) from eq. (3.60) results in

$$L_\Psi(\Psi^{n+1,j+1} - \Psi^{n+1,j}) + \theta(\Psi^{n+1,j}) - \theta(\Psi^{n+1}) + \Delta t \boldsymbol{A}_{n+1}(\Psi^{n+1,j+1} - \Psi^{n+1}) = 0, \tag{3.63}$$

which can be expressed as

$$L_\Psi(e_\Psi^{n+1,j+1} - e_\Psi^{n+1,j}) + \theta(\Psi^{n+1,j}) - \theta(\Psi^{n+1}) + \Delta t \boldsymbol{A}_{n+1}(e_\Psi^{n+1,j+1}) = 0. \tag{3.64}$$

Then multiplying with $e_\Psi^{n+1,j+1}$ (the multiplication is done element wise, and summed up after weighing by the cell mass m_i) to obtain

$$\begin{aligned} &L_\Psi\langle e_\Psi^{n+1,j+1} - e_\Psi^{n+1,j}, e_\Psi^{n+1,j+1}\rangle + \langle(\theta(\Psi^{n+1,j}) - \theta(\Psi^{n+1})), e_\Psi^{n+1,j+1}\rangle \\ &+ \Delta t\langle \boldsymbol{A}_{n+1} e_\Psi^{n+1,j+1}, e_\Psi^{n+1,j+1}\rangle = 0. \end{aligned} \tag{3.65}$$

The following inequality is needed for the finite volume method, which can be easily verified (see [27]):

$$\langle \boldsymbol{A}_{n+1} e_\Psi^{n+1,j+1}, e_\Psi^{n+1,j+1}\rangle \geq a||e_\Psi^{n+1,j+1}||^2 \tag{3.66}$$

where a not depending on Δt. The relation

$$\langle u - v, u\rangle = \frac{|u|^2}{2} + \frac{|u-v|^2}{2} - \frac{|v|^2}{2} \tag{3.67}$$

is also utilised. Combining eqs. (3.65) to (3.67), and performing some algebraic manipulations leads to

$$\left(\frac{L_\Psi}{2}+a\Delta t\right)||e_\Psi^{n+1,j+1}||^2+\frac{L_\Psi}{2}||e_\Psi^{n+1,j+1}-e_\Psi^{n+1,j}||^2+\langle(\theta(\Psi^{n+1,j})-\theta(\Psi^{n+1})),e_\Psi^{n+1,j+1}\rangle$$
$$\leq\frac{L_\Psi}{2}||e_\Psi^{n+1,j}||^2+\langle(\theta(\Psi^{n+1,j})-\theta(\Psi^{n+1})),e_\Psi^{n+1,j+1}-e_\Psi^{n+1,j}\rangle. \tag{3.68}$$

By using the monotonicity of θ, its Lipschitz continuity and the Young inequality, i.e. $|uv|\leq\frac{\epsilon}{2}|u|^2+\frac{1}{2\epsilon}|v|^2$ for all $\epsilon>0$, this further becomes

$$\left(\frac{L_\Psi}{2}+a\Delta t\right)||e_\Psi^{n+1,j+1}||^2+\frac{L_\Psi}{2}||e_\Psi^{n+1,j+1}-e_\Psi^{n+1,j}||^2+\frac{1}{L_\theta}||\theta(\Psi^{n+1,j})-\theta(\Psi^{n+1})||^2$$
$$\leq\frac{L_\Psi}{2}||e_\Psi^{n+1,j}||^2+\frac{1}{2\epsilon}||\theta(\Psi^{n+1,j})-\theta(\Psi^{n+1})||^2+\frac{\epsilon}{2}||e_\Psi^{n+1,j+1}-e_\Psi^{n+1,j}||^2, \tag{3.69}$$

with the condition on L_θ: $\frac{1}{L_\theta}\geq\frac{1}{2L_\Psi}$. From $L_\Psi>\frac{L_\theta}{2}$ and letting $\epsilon=L_\Psi$, this gives

$$\left(\frac{L_\Psi}{2}+a\Delta t\right)||e_\Psi^{n+1,j+1}||^2\leq\frac{L_\Psi}{2}||e_\Psi^{n+1,j}||^2. \tag{3.70}$$

Finally,

$$||e_\Psi^{n+1,j+1}||^2\leq\frac{L_\Psi}{(L_\Psi+2\Delta ta)}||e_\Psi^{n+1,j}||^2. \tag{3.71}$$

Equation (3.71) is clearly a contraction [24], hence proving the convergence as $||e_\Psi^{n+1,j+1}||\longrightarrow 0$ when $j\longrightarrow\infty$. □

3.4.2 Linearisation Scheme for Richards' Equation with Dynamic Capillary Pressure

The linearisation scheme for Richards' equation with dynamic capillary pressure about to be presented, is a new scheme continuing the works of M.Slodicka [37], Radu et al. [27] and F.A.Radu [40]. A similar scheme is given by Fan et al. [22], where they solve for saturation and not pressure as in this thesis.

A fully implicit temporal discretisation of Richards' equation with dynamic capillary pressure (eqs. (3.136) and (3.137)), by the backward Euler method, leads to the nonlinear system

$$\theta^{n+1}+\Delta t\boldsymbol{A}_{n+1}\Psi^{n+1}=\Delta tf^{n+1}+\theta^n, \tag{3.72}$$

$$\Delta t\Psi^{n+1}=-\Delta tp_c(\theta^{n+1})+\tau\theta^{n+1}-\tau\theta^n, \tag{3.73}$$

where $\boldsymbol{A}_{n+1}$ is the system matrix defined as (3.58). For a detailed explanation of how eqs. (3.72) and (3.73) is derived see section 3.5.3. Note that this system is coupled. The new linearisation method is considered when solving the system of equations. Iterate $j+1$ is obtained by solving

$$L_\Psi(\Psi^{n+1,j+1} - \Psi^{n+1,j}) + \theta^{n+1,j+1} + \Delta t \boldsymbol{A}_{n+1}\Psi^{n+1,j+1} = \Delta t f^{n+1} + \theta^n, \tag{3.74}$$

and

$$\Delta t \Psi^{n+1,j+1} = -\Delta t p_c(\theta^{n+1,j}) + \tau\theta^{n+1,j+1} - \tau\theta^n + L_\theta(\theta^{n+1,j+1} - \theta^{n+1,j}). \tag{3.75}$$

L_Ψ, L_θ are positive constants to be specified at a later time. The errors at iteration step $j+1$ are introduced to evaluate the convergence of the linear system

$$e_\Psi^{n+1,j+1} = \Psi^{n+1,j+1} - \Psi^{n+1}, \tag{3.76}$$

$$e_\theta^{n+1,j+1} = \theta^{n+1,j+1} - \theta^{n+1}. \tag{3.77}$$

Again, the convergence will be proved by showing that

$$||e_\Psi^{n+1,j+1}||, ||e_\theta^{n+1,j+1}|| \longrightarrow 0 \text{ when } j \longrightarrow \infty, \tag{3.78}$$

where $||\cdot||$ is the notation for the discrete L_2 norm, defined in the same manner as in section 3.4.1.

Theorem 3.2. *Assuming (A1)-(A4) and that the time step Δt is sufficiently small, and that the finite volume method satisfies* (3.66)*, the linearisation scheme* (3.74) *and* (3.75) *is (at least) linearly convergent for any $L_\Psi > 0$ and $L_\theta \geq \Delta t L_{p_c}$.*

Proof. Subtracting eqs. (3.72) and (3.73) from eqs. (3.74) and (3.75) results in

$$L_\Psi(e_\Psi^{n+1,j+1} - e_\Psi^{n+1,j}) + e_\theta^{n+1,j+1} + \Delta t \boldsymbol{A}_{n+1}(e_\Psi^{n+1,j+1}) = 0, \tag{3.79}$$

and

$$L_\theta(e_\theta^{n+1,j+1} - e_\theta^{n+1,j}) - \Delta t(p_c(\theta^{n+1,j}) - p_c(\theta^{n+1})) + \tau e_\theta^{n+1,j+1} = \Delta t e_\Psi^{n+1,j+1}. \tag{3.80}$$

Multiplying with $\Delta t e_\Psi^{n+1,j+1}$ in eq. (3.79) and $e_\theta^{n+1,j+1}$ in eq. (3.80) and then adding the results gives

$$\begin{aligned}
&\Delta t L_\Psi \langle e_\Psi^{n+1,j+1} - e_\Psi^{n+1,j}, e_\Psi^{n+1,j+1}\rangle + \Delta t \langle e_\theta^{n+1,j+1}, e_\Psi^{n+1,j+1}\rangle \\
&+ \Delta t^2 \langle \boldsymbol{A}_{n+1} e_\Psi^{n+1,j+1}, e_\Psi^{n+1,j+1}\rangle + L_\theta \langle e_\theta^{n+1,j+1} - e_\theta^{n+1,j}, e_\theta^{n+1,j+1}\rangle \\
&- \Delta t \langle p_c(\theta^{n+1,j}) - p_c(\theta^{n+1}), e_\theta^{n+1,j+1}\rangle + \tau ||e_\theta^{n+1,j+1}||^2 = \Delta t \langle e_\Psi^{n+1,j+1}, e_\theta^{n+1,j+1}\rangle.
\end{aligned} \tag{3.81}$$

Applying (3.66) and (3.67) yields

$$\begin{aligned}
&\frac{\Delta t}{2} L_\Psi ||e_\Psi^{n+1,j+1}||^2 + \frac{\Delta t}{2} L_\Psi ||e_\Psi^{n+1,j+1} - e_\Psi^{n+1,j}||^2 + \Delta t^2 a ||e_\Psi^{n+1,j+1}||^2 \\
&+ \frac{L_\theta}{2} ||e_\theta^{n+1,j+1}||^2 + \frac{L_\theta}{2} ||e_\theta^{n+1,j+1} - e_\theta^{n+1,j}||^2 - \Delta t \langle p_c(\theta^{n+1,j}) - p_c(\theta^{n+1}), e_\theta^{n+1,j}\rangle \\
&+ \tau ||e_\theta^{n+1,j+1}||^2 \leq \frac{\Delta t}{2} L_\Psi ||e_\Psi^{n+1,j}||^2 + \frac{L_\theta}{2} ||e_\theta^{n+1,j}||^2 \\
&+ \Delta t \langle p_c(\theta^{n+1,j}) - p_c(\theta^{n+1}), e_\theta^{n+1,j+1} - e_\theta^{n+1,j}\rangle.
\end{aligned} \tag{3.82}$$

Using the fact that p_c is monotone decreasing and Lipschitz continuous

$$- \langle p_c(\theta^{n+1,j}) - p_c(\theta^{n+1}), e_\theta^{n+1,j}\rangle \geq \frac{1}{L_{p_c}} ||p_c(\theta^{n+1,j}) - p_c(\theta^{n+1})||^2, \tag{3.83}$$

and applying Young's inequality with $\epsilon = L_{p_c}$, gives

$$\begin{aligned}
&\frac{\Delta t L_\Psi}{2} ||e_\Psi^{n+1,j+1}||^2 + \frac{\Delta t L_\Psi}{2} ||e_\Psi^{n+1,j+1} - e_\Psi^{n+1,j}||^2 + \Delta t^2 a ||e_\Psi^{n+1,i+1}||^2 \\
&+ \left(\frac{L_\theta}{2} + \tau\right) ||e_\theta^{n+1,j+1}||^2 + \frac{\Delta t}{L_{p_c}} ||p_c(\theta^{n+1,j}) - p_c(\theta^{n+1})||^2 \\
&+ \frac{L_\theta}{2} ||e_\theta^{n+1,j+1} - e_\theta^{n+1,j}||^2 \leq \frac{\Delta t L_\Psi}{2} ||e_\Psi^{n+1,j}||^2 + \frac{L_\theta}{2} ||e_\theta^{n+1,j}||^2 \\
&+ \frac{\Delta t}{2 L_{p_c}} ||p_c(\theta^{n+1,j}) - p_c(\theta^{n+1})||^2 + \frac{\Delta t L_{p_c}}{2} ||e_\theta^{n+1,j+1} - e_\theta^{n+1,j}||^2,
\end{aligned} \tag{3.84}$$

which in turn becomes

$$\begin{aligned}
&\frac{\Delta t L_\Psi}{2} ||e_\Psi^{n+1,j+1}||^2 + \frac{\Delta t L_\Psi}{2} ||e_\Psi^{n+1,j+1} - e_\Psi^{n+1,j}||^2 + \Delta t^2 a ||e_\Psi^{n+1,j+1}||^2 \\
&+ \left(\frac{L_\theta}{2} + \tau\right) ||e_\theta^{n+1,j+1}||^2 + \frac{\Delta t}{2 L_{p_c}} ||p_c(\theta^{n+1,j}) - p_c(\theta^{n+1})||^2 \\
&+ \left(\frac{L_\theta}{2} - \frac{\Delta t L_{p_c}}{2}\right) ||e_\theta^{n+1,j+1} - e_\theta^{n+1,j}||^2 \leq \frac{\Delta t L_\Psi}{2} ||e_\Psi^{n+1,j}||^2 + \frac{L_\theta}{2} ||e_\theta^{n+1,j}||^2,
\end{aligned} \tag{3.85}$$

with the condition on L_θ: $L_\theta \geq \Delta t L_{p_c}$. Finally, multiplying with 2 and leaving out two positive terms leads to

$$(\Delta t L_\Psi + 2\Delta t^2 a)||e_\Psi^{n+1,j+1}||^2 + (L_\theta + 2\tau)||e_\theta^{n+1,j+1}||^2 \leq \Delta t L_\Psi ||e_\Psi^{n+1,j}||^2 + L_\theta ||e_\theta^{n+1,j}||^2. \tag{3.86}$$

In order to show the convergence eq. (3.86) will be expressed on the form

$$\gamma T^{n+1,j+1} \leq \gamma_1 T^{n+1,j}, \quad \text{with} \quad \gamma \geq \gamma_1. \tag{3.87}$$

By letting

$$T^{n+1,j+1} = \Delta t L_\Psi ||e_\Psi^{n+1,j+1}||^2 + L_\theta ||e_\theta^{n+1,j+1}||^2, \tag{3.88}$$

eq. (3.86) becomes

$$T^{n+1,j+1} + 2\Delta t^2 a||e_\Psi^{n+1,j+1}||^2 + 2\tau||e_\theta^{n+1,j+1}||^2 \leq T^{n+1,j}. \tag{3.89}$$

The next step consists of defining

$$\frac{2\Delta t^2 a}{\Delta t L_\Psi}(\Delta t L_\Psi ||e_\Psi^{n+1,j+1}||^2) + \frac{2\tau}{L_\theta}(L_\theta ||e_\theta^{n+1,j+1}||^2) \geq min\left(\frac{2\Delta t a}{L_\Psi} + \frac{2\tau}{L_\theta}\right) T^{n+1,j+1}, \tag{3.90}$$

and inserting this into eq. (3.89) which gives

$$\left(min\left(\frac{2\Delta t a}{L_\Psi} + \frac{2\tau}{L_\theta}\right) + 1\right) T^{n+1,j+1} \leq T^{n+1,j}, \tag{3.91}$$

and further

$$T^{n+1,j+1} \leq \frac{1}{\left(min\left(\frac{2\Delta t a}{L_\Psi} + \frac{2\tau}{L_\theta}\right) + 1\right)} T^{n+1,j}. \tag{3.92}$$

Equation (3.92) is a contraction, hence the system converges linearly for any $L_\Psi > 0$ and $L_\theta \geq \Delta t L_{p_c}$, as $||e_\Psi^{n+1,j+1}||, ||e_\theta^{n+1,j+1}|| \longrightarrow 0$ when $j \longrightarrow \infty$. □

3.5 Discretisation of the System of Equations in Space and Time

To this point, the focus of the spatial discretisations has been on the second order in space ODE, eq. (3.12). However, the main equations to be evaluated in this thesis, given by the mathematical models (2.50)-(2.52) in section 2.4.2, are

PDEs that are second order in space and first order in time. This section will thus present the spatial and temporal discretisation of the convection-diffusion equation, the Richards equation and the equations including dynamic capillarity. The two latter being nonlinear equations undergoing additional considerations with the linearisation schemes presented in section 3.4.

3.5.1 Convection-Diffusion Equation

The convection-diffusion equation from (2.51) is on the form

$$(\theta c)_t + (-\theta D_c c_x + q(x,t)c)_x = Q(x,t), \tag{3.93}$$

where $q(x,t)$ is the water flux, $Q(x,t)$ is the source or sink term, and c=c(x,t) the concentration of the species, see section 2.1.5. D_c is the diffusion coefficient, and θ is some function

$$\theta = \theta(x,t), \tag{3.94}$$

which models the water content in the porous medium. θ and q are obtained by solving the flow equation numerically.

In this case F in the Euler implicit method, eq. (3.54), becomes

$$F(t,c(t)) = Q(x,t) + (\theta D_c c_x)_x - (q(x,t)c)_x, \tag{3.95}$$

and the approximation of the time derivative is given by the backward difference, eq. (3.4)

$$(\theta(x,t)c)_t = \frac{\theta^{n+1}c^{n+1} - \theta^n c^n}{\Delta t}, \tag{3.96}$$

where $\theta^{n+1} = \theta(x,t^{n+1})$. Thus, the implicit scheme for time step $n+1$ is

$$\theta^{n+1}c^{n+1} - \Delta t\left[(\theta^{n+1}D_c c_x^{n+1})_x - (q^{n+1}c^{n+1})_x\right] = \Delta t Q^{n+1} + \theta^n c^n. \tag{3.97}$$

To ease the notation going into the spatial discretisation, a variable D is denoted as

$$D(x,t) = \theta^{n+1}D_c, \tag{3.98}$$

and

$$d^{n+1} = -Dc_x^{n+1}. \tag{3.99}$$

Then eq. (3.93) becomes

$$\theta^{n+1}c^{n+1} + \Delta t(d_x^{n+1} + (q^{n+1}c^{n+1})_x) = \Delta t Q^{n+1} + \theta^n c^n, \tag{3.100}$$

from the linearity of the derivative.

Applying the cell-centred grid, see Figure 3.4, and integrating over each cell, $[x_{i-\frac{1}{2}}, x_{i+\frac{1}{2}}]$, results in

$$\begin{aligned}&\int_{x_{i-\frac{1}{2}}}^{x_{i+\frac{1}{2}}} \theta^{n+1}c^{n+1}\ dx + \Delta t(d_{i+\frac{1}{2}}^{n+1} - d_{i-\frac{1}{2}}^{n+1} + q_{i+\frac{1}{2}}^{n+1}c_{i+\frac{1}{2}}^{n+1} - q_{i-\frac{1}{2}}^{n+1}c_{i-\frac{1}{2}}^{n+1}) = \\ &\Delta t\int_{x_{i-\frac{1}{2}}}^{x_{i+\frac{1}{2}}} Q^{n+1}\ dx + \int_{x_{i-\frac{1}{2}}}^{x_{i+\frac{1}{2}}} \theta^{n}c^{n}\ dx,\end{aligned} \tag{3.101}$$

where e.g. $d_{i+\frac{1}{2}} = d(x_{i+\frac{1}{2}}, t^{n+1}, u(x_{i+\frac{1}{2}}, t^{n+1}))$ and $q_{i+\frac{1}{2}} = q(x_{i+\frac{1}{2}}, t^{n+1})$.

To approximate the integrals, the midpoint rule is applied the same way as in eq. (3.25). Given that x_i is the midpoint in the interval $[x_{i-\frac{1}{2}}, x_{i+\frac{1}{2}}]$ and the length of the interval is denoted by h, the integrals in eq. (3.101) are replaced by

$$\Delta t\int_{x_{i-\frac{1}{2}}}^{x_{i+\frac{1}{2}}} Q^{n+1}\ dx \approx \Delta t h Q_i^{n+1}, \tag{3.102}$$

$$\int_{x_{i-\frac{1}{2}}}^{x_{i+\frac{1}{2}}} \theta^{n+1}c^{n+1}\ dx \approx h\theta_i^{n+1}c_i^{n+1} \tag{3.103}$$

and

$$\int_{x_{i-\frac{1}{2}}}^{x_{i+\frac{1}{2}}} \theta^{n}c^{n}\ dx \approx h\theta_i^{n}c_i^{n}, \tag{3.104}$$

which leads to

$$h\theta_i^{n+1}c_i^{n+1} + \Delta t(d_{i+\frac{1}{2}}^{n+1} - d_{i-\frac{1}{2}}^{n+1} + q_{i+\frac{1}{2}}^{n+1}c_{i+\frac{1}{2}}^{n+1} - q_{i-\frac{1}{2}}^{n+1}c_{i-\frac{1}{2}}^{n+1}) = \Delta t h Q_i^{n+1} + h\theta_i^{n}c_i^{n}. \tag{3.105}$$

Since the applied grid is cell-centred, the function values are defined at the centres of the cells, leaving the values at the walls of the cells to be determined. These values are approximated by the mean of the function values of the two neighbouring cells, yielding

$$c_{i+\frac{1}{2}}^{n+1} \approx \frac{c_i^{n+1} + c_{i+1}^{n+1}}{2}, \tag{3.106}$$

for $i = 0, \ldots, N$. Also recalling from eq. (3.21) that

$$q_{i+\frac{1}{2}} = -a_{i+1}(u_{i+1} - u_i), \tag{3.107}$$

where a_i is given by eq. (3.24), for $i = 0, \ldots, N$. Inserting eq. (3.106) gives

$$q_{i+\frac{1}{2}}^{n+1} c_{i+\frac{1}{2}}^{n+1} - q_{i-\frac{1}{2}}^{n+1} c_{i-\frac{1}{2}}^{n+1} \approx q_{i+\frac{1}{2}}^{n+1} \frac{c_i^{n+1} + c_{i+1}^{n+1}}{2} - q_{i-\frac{1}{2}}^{n+1} \frac{c_{i-1}^{n+1} + c_i^{n+1}}{2}, \tag{3.108}$$

for $i = 1, \ldots, N$. Rearranging eq. (3.108) leads to

$$q_{i+\frac{1}{2}}^{n+1} c_{i+\frac{1}{2}}^{n+1} - q_{i-\frac{1}{2}}^{n+1} c_{i-\frac{1}{2}}^{n+1} \approx \frac{1}{2}(q_{i+\frac{1}{2}}^{n+1} c_{i+1}^{n+1} + (q_{i+\frac{1}{2}}^{n+1} - q_{i-\frac{1}{2}}^{n+1}) c_i^{n+1} - q_{i-\frac{1}{2}}^{n+1} c_{i-1}^{n+1}). \tag{3.109}$$

To find an expression for $d_{i+\frac{1}{2}}^{n+1}$, the procedure defined in section 3.2.2 is followed. Integrating $c_x^{n+1} = -d^{n+1}/D$ for an equidistant grid with h denoting the length of each cell, leads to

$$c_{i+1}^{n+1} - c_i^{n+1} = -d_{i+\frac{1}{2}}^{n+1} \frac{h}{2} \left(\frac{1}{D_i} + \frac{1}{D_{i+1}} \right), \tag{3.110}$$

and

$$d_{i+\frac{1}{2}}^{n+1} = -\frac{c_{i+1}^{n+1} - c_i^{n+1}}{\frac{h}{2}\left(\frac{1}{D_i} + \frac{1}{D_{i+1}}\right)}. \tag{3.111}$$

This means that

$$d_{i+\frac{1}{2}}^{n+1} - d_{i-\frac{1}{2}}^{n+1} = -\frac{c_{i+1}^{n+1} - c_i^{n+1}}{\frac{h}{2}\left(\frac{1}{D_i} + \frac{1}{D_{i+1}}\right)} + \frac{c_i^{n+1} - c_{i-1}^{n+1}}{\frac{h}{2}\left(\frac{1}{D_i} + \frac{1}{D_{i-1}}\right)}, \tag{3.112}$$

and by further letting

$$s_i = \frac{1}{\frac{h}{2}\left(\frac{1}{D_i} + \frac{1}{D_{i-1}}\right)}, \tag{3.113}$$

eq. (3.112) simplifies to

$$d_{i+\frac{1}{2}}^{n+1} - d_{i-\frac{1}{2}}^{n+1} = -s_{i+1}(c_{i+1}^{n+1} - c_i^{n+1}) + s_i(c_i^{n+1} - c_{i-1}^{n+1}). \tag{3.114}$$

Inserting eqs. (3.109) and (3.114) into eq. (3.105) yields

$$\begin{aligned} &h\theta_i^{n+1} c_i^{n+1} + \Delta t s_i (c_i^{n+1} - c_{i-1}^{n+1}) - \Delta t s_{i+1}(c_{i+1}^{n+1} - c_i^{n+1}) + \\ &\frac{\Delta t}{2}(q_{i+\frac{1}{2}}^{n+1} c_{i+1}^{n+1} + (q_{i+\frac{1}{2}}^{n+1} - q_{i-\frac{1}{2}}^{n+1}) c_i^{n+1} - q_{i-\frac{1}{2}}^{n+1} c_{i-1}^{n+1}) = \Delta t h Q_i^{n+1} + h\theta_i^n c_i^n. \end{aligned} \tag{3.115}$$

Collecting the terms and dividing by h finally leads to

$$\theta_i^{n+1}c_i^{n+1} + \frac{\Delta t}{h}\left(-s_{i+1} + \frac{q_{i+\frac{1}{2}}^{n+1}}{2}\right)c_{i+1}^{n+1} + \frac{\Delta t}{h}\left(s_i + s_{i+1} + \frac{q_{i+\frac{1}{2}}^{n+1} - q_{i-\frac{1}{2}}^{n+1}}{2}\right)c_i^{n+1} - \frac{\Delta t}{h}\left(s_i + \frac{q_{i-\frac{1}{2}}^{n+1}}{2}\right)c_{i-1}^{n+1} = \Delta t Q_i^{n+1} + \theta_i^n c_i^n. \tag{3.116}$$

This is a linear system discretised with respect to both space and time, which is implemented and solved numerically for c_i^{n+1}, $i = 1, \ldots, N$, $n = 0, \ldots, T$.

3.5.2 Standard Richards' Equation

The standard Richards equation is given by

$$(\theta(\Psi))_t - (K(\Psi)(\Psi(x,t) + x)_x)_x = f(x,t), \tag{3.117}$$

where $\Psi(x,t)$ is the pressure head, $f(x,t)$ is the source or sink term divided by the density ρ, (see eq. (2.35)), and x denotes the height against the reference level (*datum*). $\theta(\Psi)$ and $K(\Psi)$ are nonlinear functions given by some parameterisation. Nonlinear equations, as is the case for the Richards equation, need to be linearised in order to be solved by the means of numerical methods. The linearisation scheme presented in section 3.4 is therefore applied, in order to compute the linear, discretised system needed for it to be solved numerically.

Starting with the temporal discretisation the backward Euler scheme (eq. (3.55)) is applied, where

$$F(t, \Psi(t)) = f(x,t) + (K(\Psi)(\Psi(x,t) + x)_x)_x, \tag{3.118}$$

which leads to

$$\theta(\Psi^{n+1}) - \theta(\Psi^n) - \Delta t(K(\Psi^{n+1})\Psi_x^{n+1})_x - \Delta t(K(\Psi^{n+1}))_x = \Delta t f^{n+1}, \tag{3.119}$$

as the implicit scheme for time step $n+1$, where $\Psi^{n+1} = \Psi(x, t^{n+1})$. The standard approach to solving this system is to apply Newton's method. However, as mentioned in section 3.4, this method has several drawbacks. Instead applying

the robust linearisation method given, yields

$$L_\Psi(\Psi^{n+1,j+1} - \Psi^{n+1,j}) + \theta(\Psi^{n+1,j}) - \theta(\Psi^n) - \Delta t(K(\Psi^{n+1,j})\Psi_x^{n+1,j+1})_x - \Delta t K_x(\Psi^{n+1,j}) = \Delta t f^{n+1}, \tag{3.120}$$

for obtaining iteration step $j+1$, where L_Ψ is some positive constant. Rearranging eq. (3.120) so that the known values at previous time and iteration steps are located on the right hand side of the equation, leads to

$$L_\Psi \Psi^{n+1,j+1} - \Delta t(K(\Psi^{n+1,j})\Psi_x^{n+1,j+1})_x = \Delta t f^{n+1} + L_\Psi \Psi^{n+1,j} - \theta(\Psi^{n+1,j}) + \theta(\Psi^n) + \Delta t K_x(\Psi^{n+1,j}), \tag{3.121}$$

concluding the temporal discretisation and the iterative approach.

The first step in the spatial discretisation is to define the flux as

$$q = -K(\Psi^{n+1,j})\Psi_x^{n+1,j+1}, \tag{3.122}$$

then eq. (3.120) becomes

$$L_\Psi \Psi^{n+1,j+1} + \Delta t q_x = \Delta t f^{n+1} + L_\Psi \Psi^{n+1,j} - \theta(\Psi^{n+1,j}) + \theta(\Psi^n) + \Delta t K_x(\Psi^{n+1,j}). \tag{3.123}$$

Applying the cell-centred grid, see fig. 3.4, and integrating over each cell, $[x_{i-\frac{1}{2}}, x_{i+\frac{1}{2}}]$, results in

$$L_\Psi \int_{x_{i-\frac{1}{2}}}^{x_{i+\frac{1}{2}}} \Psi^{n+1,j+1}\,dx + \Delta t(q_{i+\frac{1}{2}} - q_{i-\frac{1}{2}}) = \Delta t \int_{x_{i-\frac{1}{2}}}^{x_{i+\frac{1}{2}}} f^{n+1} + L_\Psi \int_{x_{i-\frac{1}{2}}}^{x_{i+\frac{1}{2}}} \Psi^{n+1,j}\,dx - \int_{x_{i-\frac{1}{2}}}^{x_{i+\frac{1}{2}}} \theta(\Psi^{n+1,j})\,dx + \int_{x_{i-\frac{1}{2}}}^{x_{i+\frac{1}{2}}} \theta(\Psi^n)\,dx + \Delta t(K_{i+\frac{1}{2}}(\Psi^{n+1,j}) - K_{i-\frac{1}{2}}(\Psi^{n+1,j})). \tag{3.124}$$

As in section 3.5.1, eqs. (3.103) to (3.105), the integrals of eq. (3.124) are approximated by the midpoint rule. Inserting these approximations into eq. (3.124), recalling that the grid is equidistant with $h = \Delta x_i$, gives

$$L_\Psi h\Psi_i^{n+1,j+1} + \Delta t(q_{i+\frac{1}{2}} - q_{i-\frac{1}{2}}) = \Delta t h f_i^{n+1} + L_\Psi h\Psi_i^{n+1,j} - h\theta_i(\Psi^{n+1,j}) + h\theta_i(\Psi^n) + \Delta t(K_{i+\frac{1}{2}}(\Psi^{n+1,j}) - K_{i-\frac{1}{2}}(\Psi^{n+1,j})), \tag{3.125}$$

where $\theta_i(\Psi^{n+1,j}) = \theta(\Psi_i^{n+1,j})$.

To determine the values at the walls of the cells, the mean of the function values of the two neighbouring cells is computed so that

$$K_{i+\frac{1}{2}}(\Psi^{n+1,j}) \approx \frac{K_i(\Psi^{n+1,j}) + K_{i+1}(\Psi^{n+1,j})}{2} \tag{3.126}$$

for $i = 0, \ldots, N$, and

$$K_{i-\frac{1}{2}}(\Psi^{n+1,j}) \approx \frac{K_{i-1}(\Psi^{n+1,j}) + K_i(\Psi^{n+1,j})}{2}, \tag{3.127}$$

for $i = 1, \ldots, N$. This gives

$$\begin{aligned} &\Delta t(K_{i+\frac{1}{2}}(\Psi^{n+1,j}) - K_{i-\frac{1}{2}}(\Psi^{n+1,j})) \\ &\approx \Delta t \left(\frac{K_i(\Psi^{n+1,j}) + K_{i+1}(\Psi^{n+1,j})}{2} - \frac{K_{i-1}(\Psi^{n+1,j}) + K_i(\Psi^{n+1,j})}{2} \right) \end{aligned} \tag{3.128}$$

for $i = 1, \ldots, N$. Subtracting the common terms yield

$$\Delta t(K_{i+\frac{1}{2}}(\Psi^{n+1,j}) - K_{i-\frac{1}{2}}(\Psi^{n+1,j})) \approx \frac{\Delta t}{2}(K_{i+1}(\Psi^{n+1,j}) - K_{i-1}(\Psi^{n+1,j})). \tag{3.129}$$

The expression for $q_{i+\frac{1}{2}}$ is found by applying the TPFA scheme, see section 3.2.2. Integrating $\Psi_x^{n+1,j+1} = -q/K(\Psi^{n+1,j})$ for an equidistant grid with h denoting the length of each cell, leads to

$$\Psi_{i+1}^{n+1,j+1} - \Psi_i^{n+1,j+1} = -q_{i+\frac{1}{2}} \frac{h}{2} \left(\frac{1}{K_i} + \frac{1}{K_{i+1}} \right), \tag{3.130}$$

and

$$q_{i+\frac{1}{2}} = -\frac{\Psi_{i+1}^{n+1,j+1} - \Psi_i^{n+1,j+1}}{\frac{h}{2}\left(\frac{1}{K_i} + \frac{1}{K_{i+1}} \right)}. \tag{3.131}$$

This means that

$$q_{i+\frac{1}{2}} - q_{i-\frac{1}{2}} = -\frac{\Psi_{i+1}^{n+1,j+1} - \Psi_i^{n+1,j+1}}{\frac{h}{2}\left(\frac{1}{K_i} + \frac{1}{K_{i+1}} \right)} + \frac{\Psi_i^{n+1,j+1} - \Psi_{i-1}^{n+1,j+1}}{\frac{h}{2}\left(\frac{1}{K_i} + \frac{1}{K_{i-1}} \right)} \tag{3.132}$$

and by further letting

$$a_i = \frac{1}{\frac{h}{2}\left(\frac{1}{K_i} + \frac{1}{K_{i-1}} \right)}$$

from eq. (3.24), eq. (3.132) simplifies to

$$q_{i+\frac{1}{2}} - q_{i-\frac{1}{2}} = -a_{i+1}(\Psi_{i+1}^{n+1,j+1} - \Psi_i^{n+1,j+1}) + a_i(\Psi_i^{n+1,j+1} - \Psi_{i-1}^{n+1,j+1}). \tag{3.133}$$

Inserting eqs. (3.129) and (3.133) into eq. (3.125) yields

$$L_\Psi h\Psi_i^{n+1,j+1} + \Delta t a_i(\Psi_i^{n+1,j+1} - \Psi_{i-1}^{n+1,j+1}) - \Delta t a_{i+1}(\Psi_{i+1}^{n+1,j+1} - \Psi_i^{n+1,j+1}) = \Delta t h f_i^{n+1} + L_\Psi h\Psi_i^{n+1,j} - h\theta_i(\Psi^{n+1,j}) + h\theta_i(\Psi^n) + \frac{\Delta t}{2}(K_{i+1}(\Psi^{n+1,j}) - K_{i-1}(\Psi^{n+1,j})). \tag{3.134}$$

Collecting the terms and dividing by h finally leads to

$$L_\Psi \Psi_i^{n+1,j+1} - \frac{\Delta t}{h} a_i \Psi_{i-1}^{n+1,j+1} + \frac{\Delta t}{h}(a_i + a_{i+1})\Psi_i^{n+1,j+1} - \frac{\Delta t}{h} a_{i+1}\Psi_{i+1}^{n+1,j+1} = \Delta t f_i^{n+1} + L_\Psi \Psi_i^{n+1,j} - \theta_i(\Psi^{n+1,j}) + \theta_i(\Psi^n) + \frac{\Delta t}{2h}(K_{i+1}(\Psi^{n+1,j}) - K_{i-1}(\Psi^{n+1,j})). \tag{3.135}$$

The original nonlinear system is now a linear system discretised with respect to space and time, and is implemented and solved numerically for $\Psi_i^{n+1,j+1}$, i=1,. . . ,N, $n = 1, \ldots, T$, $j = 1, \ldots, J$.

3.5.3 Richards' Equation with Dynamic Capillary Pressure

In the case of dynamic capillary pressure, two equations are considered. These are

$$\theta_t - (K(\theta)(\Psi(x,t) + x)_x)_x = f(x,t), \tag{3.136}$$

and

$$\Psi(x,t) = -p_c(\theta) + \tau(\theta)\frac{\partial \theta}{\partial t}, \tag{3.137}$$

where the first equation is the Richards equation considered in section 3.5.2, and the second is the extension accommodating dynamic capillary pressure. $p_c(\theta)$ is the capillary pressure and $\tau(\theta) = \tau$ some constant. Both equations are nonlinear and need to be linearised with the method described in section 3.4. Equations (3.136) and (3.137) are coupled, meaning one cannot be solved without the other.

The implicit numerical schemes when applying the backward Euler method (eq. (3.55)), are

$$\theta^{n+1} - \theta^n - \Delta t(K(\theta^{n+1})\Psi_x^{n+1})_x - \Delta t(K(\theta^{n+1}))_x = \Delta t f^{n+1} \tag{3.138}$$

from eq. (3.119), and

$$\Delta t \Psi^{n+1} = -\Delta t p_c(\theta^{n+1}) + \tau(\theta^{n+1} - \theta^n). \tag{3.139}$$

Again, the robust iterative scheme for Richards' equation is previously given by eq. (3.120) in section 3.5.2

$$\begin{aligned} &L_\Psi(\Psi^{n+1,j+1} - \Psi^{n+1,j}) + \theta^{n+1,j+1} - \theta^n - \Delta t(K(\theta^{n+1,j})\Psi_x^{n+1,j+1})_x \\ &- \Delta t K_x(\theta^{n+1,j}) = \Delta t f^{n+1}, \end{aligned} \tag{3.140}$$

while the iterative scheme for the dynamic capillary pressure becomes

$$\Delta t\Psi^{n+1,j+1} = -\Delta t p_c(\theta^{n+1,j}) + \tau\theta^{n+1,j+1} - \tau\theta^n + L_\theta(\theta^{n+1,j+1} - \theta^{n+1,j}), \tag{3.141}$$

when applying the linearisation method. L_Ψ and L_θ are positive constants.

Remark. In the case of a non-constant τ, i.e. $\tau = \tau(\theta)$, the iterative scheme (3.141) above becomes

$$\Delta t\Psi^{n+1,j+1} = -\Delta t p_c(\theta^{n+1,j}) + \tau(\theta^{n+1,j})\theta^{n+1,j+1} - \tau(\theta^{n+1,j})\theta^n + L_\theta(\theta^{n+1,j+1} - \theta^{n+1,j}). \tag{3.142}$$

This scheme was also implemented and results are presented in section 4.2.

In order to solve the coupled system, eq. (3.141) is first solved with respect to $\theta^{n+1,j+1}$, before being inserted into eq. (3.140). Rearranging eq. (3.141) gives

$$\theta^{n+1,j+1} = \frac{1}{(\tau + L_\theta)}(\Delta t\Psi^{n+1,j+1} + \Delta t p_c(\theta^{n+1,j}) + \tau\theta^n + L_\theta\theta^{n+1,j}), \tag{3.143}$$

and by inserting the relation in eq. (3.140), it follows that

$$\begin{aligned} &L_\Psi(\Psi^{n+1,j+1} - \Psi^{n+1,j}) \\ &+ \frac{1}{(\tau + L_\theta)}(\Delta t\Psi^{n+1,j+1} + \Delta t p_c(\theta^{n+1,j}) + \tau\theta^n + L_\theta\theta^{n+1,j}) \\ &- \theta^n - \Delta t(K(\theta^{n+1,j})\Psi_x^{n+1,j+1})_x - \Delta t K_x(\theta^{n+1,j}) = \Delta t f^{n+1}. \end{aligned} \tag{3.144}$$

Moving the known terms from the previous time and iteration steps to the right hand side og the equation, leads to

$$\begin{aligned} &L_\Psi\Psi^{n+1,j+1} + \frac{\Delta t}{(\tau + L_\theta)}\Psi^{n+1,j+1} - \Delta t(K(\theta^{n+1,j})\Psi_x^{n+1,j+1})_x \\ &= \Delta t f^{n+1} + L_\Psi\Psi^{n+1,j} - \frac{\Delta t}{(\tau + L_\theta)}p_c(\theta^{n+1,j}) - \frac{\tau}{(\tau + L_\theta)}\theta^n \\ &- \frac{L_\theta}{(\tau + L_\theta)}\theta^{n+1,j} + \theta^n + \Delta t K_x(\theta^{n+1,j}). \end{aligned} \tag{3.145}$$

Integrating each term over each cell $[x_{i-\frac{1}{2}}, x_{i+\frac{1}{2}}]$, inserting eqs. (3.129) and (3.133) from section 3.5.2 and approximating the remaining integrals using the midpoint rule, see eqs. (3.102) to (3.104), yields

$$\begin{aligned} &L_\Psi h\Psi_i^{n+1,j+1} + \frac{\Delta t h}{(\tau + L_\theta)}\Psi_i^{n+1,j+1} + \Delta t a_i(\Psi_i^{n+1,j+1} - \Psi_{i-1}^{n+1,j+1}) \\ &- \Delta t a_{i+1}(\Psi_{i+1}^{n+1,j+1} - \Psi_i^{n+1,j+1}) = \Delta t h f_i^{n+1} + L_\Psi h\Psi_i^{n+1,j} \\ &- \frac{\Delta t h}{(\tau + L_\theta)}p_{c_i}(\theta^{n+1,j}) - \frac{\tau h}{(\tau + L_\theta)}\theta_i^n - \frac{L_\theta h}{(\tau + L_\theta)}\theta_i^{n+1,j} + h\theta_i^n \\ &+ \frac{\Delta t}{2}(K_{i+1}(\theta^{n+1,j}) - K_{i-1}(\theta^{n+1,j})). \end{aligned} \tag{3.146}$$

Finally, collecting the terms and dividing by h, gives

$$\begin{aligned} &\left(L_\Psi + \frac{\Delta t}{(\tau + L_\theta)}\right)\Psi_i^{n+1,j+1} - \frac{\Delta t}{h}a_i\Psi_{i-1}^{n+1,j+1} + \frac{\Delta t}{h}(a_i + a_{i+1})\Psi_i^{n+1,j+1} \\ &- \frac{\Delta t}{h}a_{i+1}\Psi_{i+1}^{n+1,j+1} = \Delta t f_i^{n+1} + L_\Psi\Psi_i^{n+1,j} - \frac{\Delta t}{(\tau + L_\theta)}p_{c_i}(\theta^{n+1,j}) \\ &+ \left(1 - \frac{\tau}{(\tau + L_\theta)}\right)\theta_i^n - \frac{L_\theta}{(\tau + L_\theta)}\theta_i^{n+1,j} + \frac{\Delta t}{2h}(K_{i+1}(\theta^{n+1,j}) - K_{i-1}(\theta^{n+1,j})) \end{aligned} \tag{3.147}$$

Equation (3.147) represents the linear, discretised system for the case with Richards' equation and dynamic capillary pressure. This system is implemented and solved numerically for $\Psi_i^{n+1,j+1}$, i=1,. . . ,N, $n = 1, \ldots, T$, $j = 1, \ldots, J$.

3.6 Implementation

The numerical computations based on the discretised system of equations derived in sections 3.5.1 to 3.5.3 are performed using the software MATLAB. The discretised equations are implemented using functions where values of all known variables, as well as initial and boundary conditions, are defined. Approximated solutions of the unknown variables are computed at time step $n+1$ as time evolves. The approximations will improve for each time step in the case of convergence of the system.

As well as being evaluated at each time step, the solutions of the linearised Richards' equation, with and without dynamic capillary pressure are evaluated at each iteration step until some stopping criteria is met. There are two possible types of stopping criteria [24]. One based on evaluating the residual and the other

is based on the increment. In both cases a fixed tolerance on the approximated solution, ε, is defined. When considering the residual approach, the iterative process terminates at the first step i where $||f(\Psi^{n+1,i})|| < \varepsilon$. While when evaluating the increment, the iterative process terminates when $||\Psi^{n+1,i+1} - \Psi^{n+1,i}|| < \varepsilon$. The latter is applied in the numerical schemes constructed for this thesis. In the possible event that the method does not converge, a security measure to prevent an indefinite continuation of the iterative process is included. That is, after a maximum number of iteration steps set high enough to ensure a good approximation of the solution in the case of convergence, the method is terminated.

The linear system at each time step can be solved by the means of a direct solver or an iterative one (e.g. Jacobi or Gauss-Seidel, [24, 25]). In this work a direct solver is utilised. The problem being one dimensional gives rise to relatively small linear systems, making the use of a direct solver convenient.

Finally, the solutions of Ψ (pressure), θ (water content) and c (concentration) as well as the convergence history of the linearisation schemes, are presented graphically at certain time and grid steps.

Chapter 4

Numerical Results

This chapter is devoted to presenting the results attained from numerical simulations constructed on the basis of the theoretical framework and discretised models described in preceding chapters. The first section gives the results of a numerical convergence test, where a constructed analytical solution was applied to verify the convergence of the numerical method. Section 4.2 contains the numerical results produced when the developed numerical schemes are applied to the transport problem. Comparing the results with and without dynamic capillary pressure is the main focus. Also, in order to confirm the statements made about the linearisation schemes in section 3.4, the convergence history displaying the number of iterations for different grid lengths h are presented. From this, it will be shown that the linearisation schemes are at least linearly convergent, robust and indeed independent of mesh size.

4.1 Convergence of the Numerical Solution for an Academical Example

The purpose of this section is to show that the numerical solution of the system converges. To do so a numerical test is presented, based the approach described in [38], section 3. The numerical simulations are performed by choosing a simple analytical solution that satisfies the given initial and boundary conditions and by adjusting the functions so that this chosen solution corresponds to the exact solution of the equation. The numerical solutions are then compared to the analytical solution by computing the L^2 error.

The convergence test is performed on (2.50) with gravitation and a source term

$$\partial_t \theta(\Psi) - \partial_x (K(\Psi)\partial_x(\Psi + x)) = f(x,t) \text{ in } (0,T) \times (0,1), \tag{4.1}$$

with final time $T = 1$. For the numerical test $L_\Psi = 0.1$ and the coefficient functions $\theta(\Psi), K(\Psi)$ are set to

$$\theta(\Psi) = \frac{1-\Psi^2}{2}, \tag{4.2}$$

$$K(\Psi) = 1 - \Psi^2, \tag{4.3}$$

The initial condition is given by

$$\Psi|_{t=0} = 0, \tag{4.4}$$

and Neumann boundary conditions are applied at both end points of the interval

$$q = K(x=0)t, \tag{4.5}$$

$$q = -K(x=1)t. \tag{4.6}$$

Note that tests with homogeneous Dirichlet boundary conditions ($\Psi|_{x=0} = \Psi|_{x=1} = 0$) were also conducted, giving the same convergence results.

Constructing an analytical solution for $\Psi(x,t)$ that satisfies the given initial and boundary conditions yields

$$\Psi_{ana}(x,t) = -tx(1-x). \tag{4.7}$$

To find the source term, eqs. (4.2) and (4.3) are inserted into eq. (4.1) and the partial derivatives are calculated from

$$f(x,t) = \left(\frac{1-\Psi_{ana}^2(x,t)}{2}\right)_t - ((1-\Psi_{ana}^2(x,t))(\Psi_{ana_x}(x,t)+1))_x, \tag{4.8}$$

which becomes

$$f(x,t) = -tx^2(1-x)^2 + 2(t^3x(5x^3-10x^2+6x-1)-t) + (2t^2x(2x^2-3x+1)), \tag{4.9}$$

when Ψ_{ana} is defined by eq. (4.7). Inserting eq. (4.9) into eq. (4.1) gives the equation to be solved in the numerical convergence test.

Solving the equation given by eqs. (4.1) and (4.9) numerically, yields numerical solutions which can be compared to the analytical solution of eq. (4.7). The

procedure for solving Richards' equation by the means of a numerical method is described in section 3.5.2. The Neumann boundary conditions are treated as in section 3.2.3.

To compare the numerical solutions to the analytical one, the L_2 norm is computed as a measure of the difference between the two. Recalling that the L_2 norm [5, 21, 24, 25] is defined as

$$||\Psi||_2 = \left(\int |\Psi|^2 \, dx \right)^{\frac{1}{2}}, \tag{4.10}$$

for a function Ψ. The error is computed as

$$\boldsymbol{E} = ||\Psi_{ana}(x,T) - \Psi_{num}(x,T)||_2, \tag{4.11}$$

where $\Psi_{ana}(x,T)$ and $\Psi_{num}(x,T)$ is the analytical and numerical solution respectively. $t = T$ for $t \in [0,1]$ represents the final time, thus $T = 1$. The squared error is given by

$$\boldsymbol{E}^2 = ||\Psi_{ana}(x,T) - \Psi_{num}(x,T)||_2^2 = \int_0^1 |\Psi_{ana}(x,T) - \Psi_{num}(x,T)|^2 \, dx, \tag{4.12}$$

for $x \in [0,1]$. To solve the equations numerically a cell-centered grid is applied to the interval $[0,1]$, dividing it into subintervals or cells with midpoints $x_i,\ i = 0, \ldots, n$, see chapter 3. Integrating over each cell $[x_{i-\frac{1}{2}}, x_{i+\frac{1}{2}}]$ gives

$$\boldsymbol{E}^2 = \sum_{i=1}^{n} \int_{x_{i-\frac{1}{2}}}^{x_{i+\frac{1}{2}}} |\Psi_{ana}(x,T) - \Psi_{num}(x,T)|^2 \, dx, \tag{4.13}$$

which is becomes

$$\boldsymbol{E}^2 \simeq \sum_{i=1}^{n} h |\Psi_{ana}(x_i,T) - \Psi_{num}(x_i,T)|^2, \tag{4.14}$$

when the integrals are approximated using the midpoint rule with h representing the uniform length of each cell.

The computations are performed on a uniform grid with $h = \Delta t = 0.1$ and halving the grid size (h) and time step (Δt) successively. Figure 4.1 show the solutions for $h = 0.1, 0.05, 0.025, 0.0125, 0.0625$. The numerical solutions for pressure Ψ are compared to the analytical solution marked with blue stars, and it is clear that the numerical solution converges to the analytical one, due to the decreasing difference in the solutions for decreasing grid and time steps.

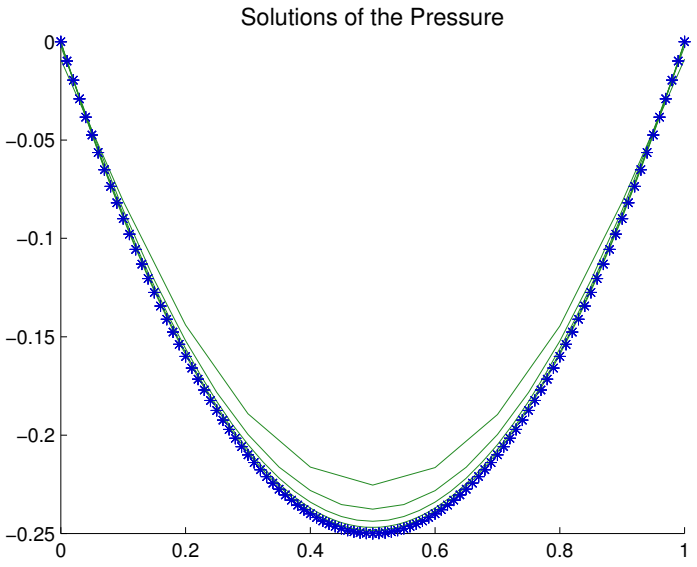

FIGURE 4.1: Numerical solutions for $h = 0.1, 0.05, 0.025, 0.0125, 0.0625$ compared to the analytical solution marked by stars.

According to *Theorem 1* in [38], $\boldsymbol{E} \leq C(\Delta t + h)$ with C constant not depending on the discretisation parameters Δt and h. The results are presented in table 4.1. As predicted in Theorem 1, the reduction of the error $\mathbf{E}$ is of factor 2, which means a convergence of $O(\Delta t + h)$ or $O(\Delta t^2 + h^2)$ for $\mathbf{E^2}$.

TABLE 4.1: Errors $\mathbf{E}$ for different h

Time step (Δt)	Step length (h)	Error ($\mathbf{E}$)	Reduction
0.1	0.1	0.018378609390458	-
0.05	0.05	0.009022002647100	2.037087563520698
0.025	0.025	0.004505633495526	2.002382718447396
0.0125	0.0125	0.002254288598985	1.998694176759216
0.00625	0.00625	0.001127719602277	1.998979705977481

4.2 Numerical Simulations

Having established the convergence of the method, it can be used to perform numerical simulations for the transport problem with and without including dynamic capillary pressure. The numerical results of these simulations are presented in section 4.2.1. To evaluate the convergence of the linearisation methods, the convergence history of the schemes are presented in section 4.2.2.

4.2.1 Numerical Solutions of Flow and Transport

The equations that are considered in the numerical simulations are defined in (2.50)-(2.52), and are restated below.

$$(\theta(\Psi))_t - (K(\theta(\Psi))(\Psi + x)_x)_x = f(x,t),$$

is again the standard Richards equation, where $\theta(\Psi), K(\theta(\Psi)))$ are assumed to be constitutive relations given by the van Genuchten-Mualem parameterisation, see section 2.2.4,

For $\Psi \leq 0$

$$\theta(\Psi) = \theta_R + (\theta_S - \theta_R)\left[\frac{1}{1+(-\alpha\Psi)^n}\right]^{\frac{n-1}{n}},$$
$$K(\theta(\Psi)) = K_S \frac{\left[1 - (-\alpha\Psi)^{n-1}\left[1+(-\alpha\Psi)^n\right]^{\frac{1-n}{n}}\right]^2}{\left[1+(-\alpha\Psi)^n\right]^{\frac{n-1}{2n}}}.$$

For $\Psi > 0$

$$\theta = \theta_S,$$
$$K = K_S.$$

Unless otherwise stated, the van Genuchten-Mualem formula is used to compute the hydraulic conductivity K. Referred to as non-constant $K(\theta)$.

To include dynamic capillarity, recall that the extension

$$\tau(\theta)\partial_t\theta(\Psi) = \Psi + p_c(\theta),$$

replaces the partial derivative of θ with respect to t in Richards' equation. For the first case considered, $\tau(\theta) = \tau$ is some constant not depending on θ. Also recall that for the case with dynamic capillary pressure $\theta \neq \theta(\Psi)$ (and $K = K(\theta)$).

To model the transport of the dissolved substance, the convection-diffusion equation given by

$$(\theta c)_t + (-\theta D_c c_x + q(x,t)c)_x = Q(x,t),$$

is coupled to the flow equations.

The spatial domain range from $x \in [0,1]$, where $x = 1$ corresponds to the ground surface. On this interval, the initial condition when $t = 0$ and boundary conditions

for $x = 0$ and $x = 1$ are defined. For the standard and non-standard Richards' equation, the boundary conditions are set to be Dirichlet for the left boundary and Neumann for the right boundary, so that

$$\begin{aligned} \Psi(0,t) &= -1, \\ q(1,t) &= -3 \times 10^{-3}. \end{aligned}$$

For the transport problem, a homogeneous initial condition,

$$c(x,0) = 0,$$

is given and the boundary conditions are defined as Dirichlet conditions for both boundaries,

$$\begin{aligned} c(0,t) &= 0, \\ c(1,t) &= 1. \end{aligned}$$

The known variables in the van Genuchten-Mualem parameterisation are defined by the residual water content $\theta_R = 0.026$ and the saturated water content $\theta_S = 0.420$. Further, $\alpha = 0.95$, $n = 1.9$ and the saturated hydraulic conductivity $K_S = 2 \times 10^{-2}$. These values are based on realistic values found in the PhD thesis of E.Schneid [43]. Note that the magnitude of the variables corresponds to values found in i.e. Hassanizadeh et al. [39] and Fučík et al. [42], when converting from seconds into days. The latter being the time scale in this thesis. The diffusion coefficient $D_c = 10^{-1}$.

In the following, two examples are considered when computing the numerical results. Boundary conditions, the initial condition for the convection-diffusion equation and known variables remain the same, while the initial condition for the Richards equation is adjusted.

Example I

The initial condition for the pressure Ψ is given by

$$\Psi(x,0) = -x - 1,$$

in order to model the water flow in the strictly unsaturated region. This is to ensure the validity of assumption (A2) in section 3.4.1. For the case when both the saturated and the unsaturated region is included in the model, the given $p_c(\theta)$ is not Lipschitz continuous.

When computing the standard Richards equation $L_\Psi = 0.07$, while in the case with dynamic capillary pressure $L_\Psi = 0.001$, $L_\theta = 1$ and $\tau = 20$. With the parameters and conditions defined above, simulations are performed with step size $h = 0.005$ and time step $\Delta t = 0.01$.

The numerical solutions for the pressure Ψ and water content θ with and without dynamic capillary pressure for constant $K = K_S$, are given in Figure 4.2. In Figure 4.3 solutions of the same variables but for non-constant $K(\theta)$ are presented. The solutions are shown for $t = 0.01\,(T_1)$, $t = 0.5\,(T_{im})$ and $t = 1\,(T_{end})$.

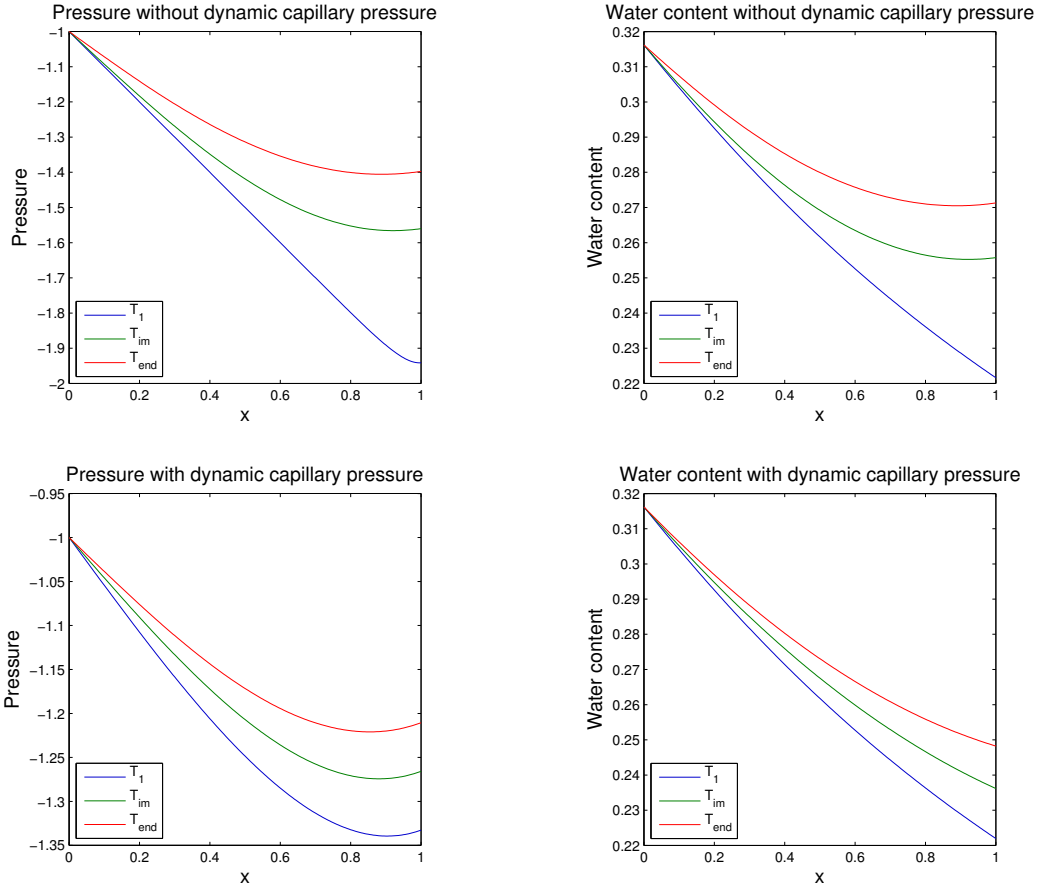

FIGURE 4.2: Pressure and water content profiles for the standard Richards equation (top), and with the influence of dynamic capillary pressure (bottom). Computations are done with constant $K = K_S$, $\tau = 20$ at time $T_1 = 0.01$, $T_{im} = 0.5$, $T_{end} = 1$.

Nonhomogeneous Neumann boundary conditions, as defined on the right boundary of the domain (the assumed ground surface), means there is a flow or flux across the boundary. In other words, the pressure is increased at the boundary which is the same as water being pumped into the domain. The nonhomogeneous Dirichlet condition gives the value of the solution at the left boundary. The given value is a

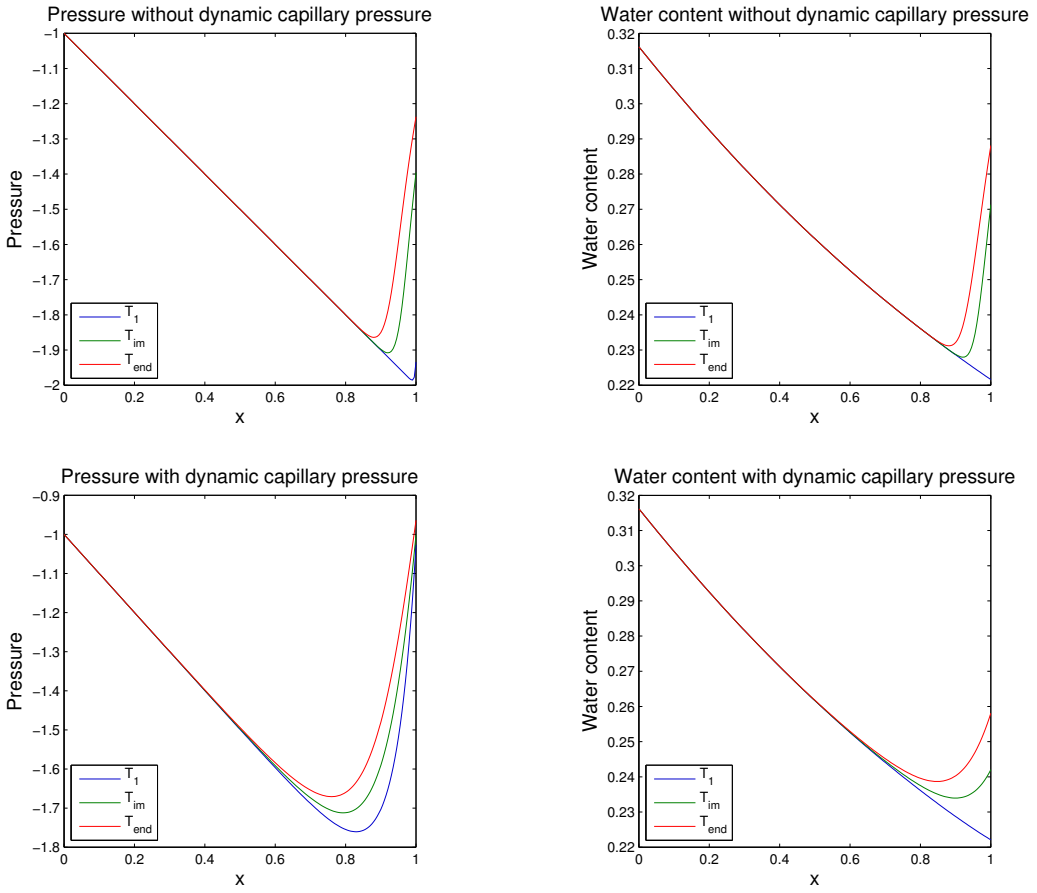

FIGURE 4.3: Pressure and water content profiles for the standard Richards equation (top), and with the influence of dynamic capillary pressure (bottom). Computations are done with non-constant $K(\theta)$ and constant $\tau = 20$ at time $T_1 = 0.01$, $T_{im} = 0.5$, $T_{end} = 1$.

result of the chosen initial condition which as mentioned previously, is a measure to ensure Lipschitz continuous $p_c(\theta)$.

As time evolves there is an increase in pressure and water content throughout the domain. The observed increase is larger in the case with constant $K = K_S$ than in the case where the van Genuchten-Mualem parameterisation for the hydraulic conductivity is applied. This is true for both the pressure and the water content profiles. As will be evident shortly, this effects the transport of the dissolved substance. The dynamic effects are obvious in both cases (constant and non-constant K), and a clear difference between the standard and non-standard profiles for pressure and water content is seen.

In Figure 4.4 numerical solutions of Richards' equation *with* dynamic capillary pressure for varying values of $\tau(\theta)$ are presented.

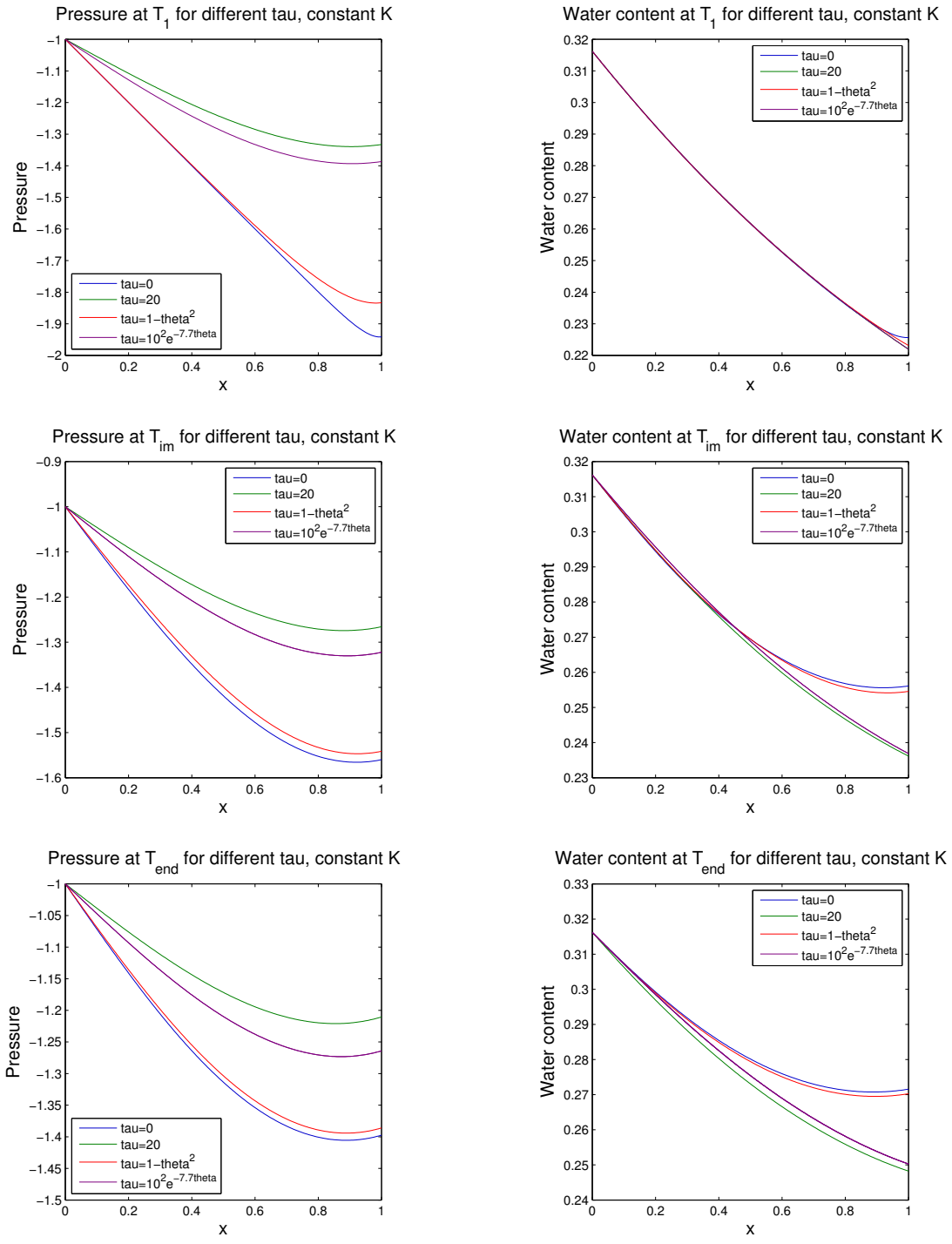

FIGURE 4.4: Pressure and water content profiles for different values of τ, $\tau = 0,\ 20,\ 1-\theta^2,\ 10^2 \times e^{-7.7\theta}$. Computations are done with constant $K = K_S$ at time $T_1 = 0.01$ (top), $T_{im} = 0.5$ (middle), $T_{end} = 1$ (bottom).

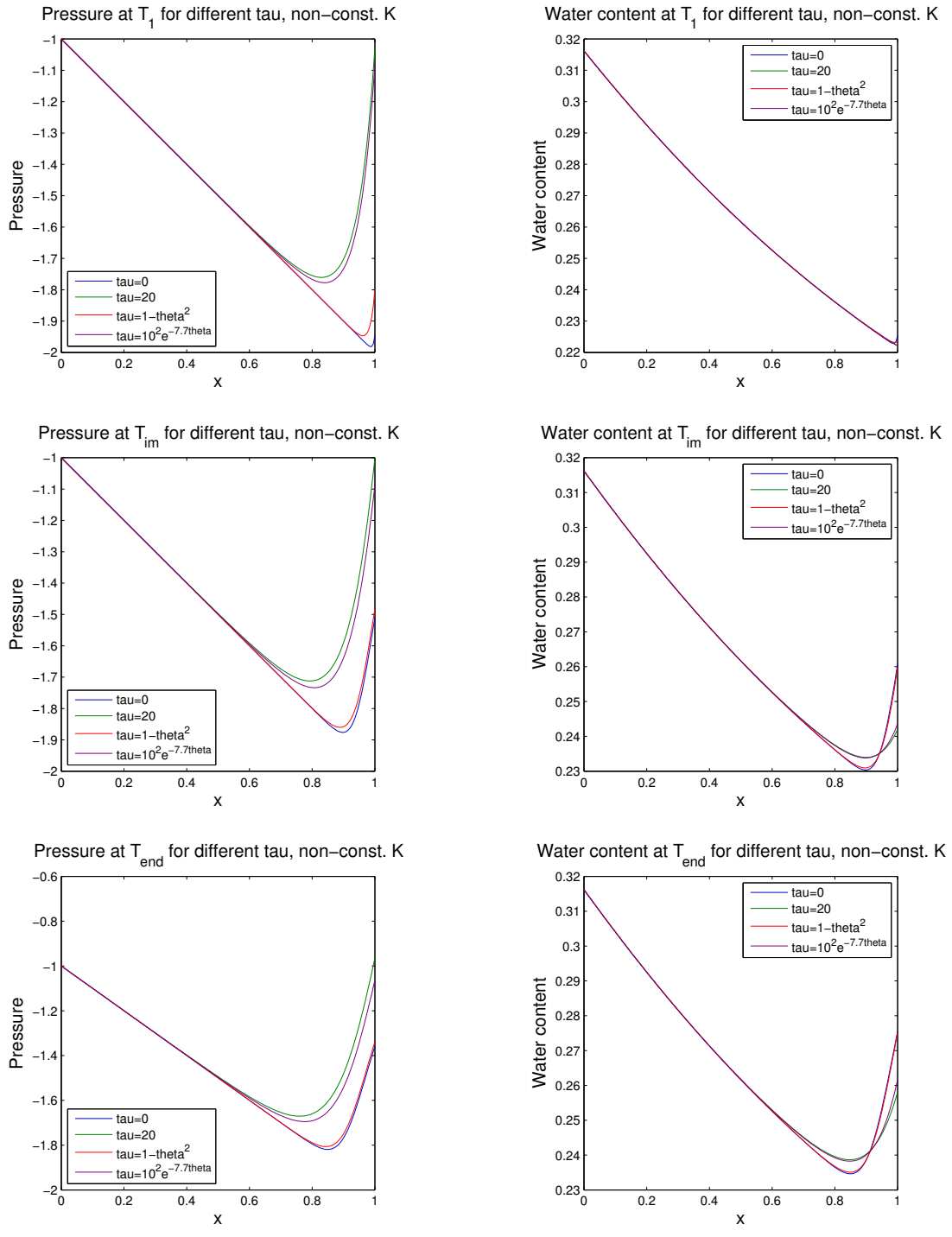

FIGURE 4.5: Pressure and water content profiles for different values of τ, $\tau = 0,\ 20,\ 1-\theta^2,\ 10^2 \times e^{-7.7\theta}$. Computations are done with non-constant $K(\theta)$ at time $T_1 = 0.01$ (top), $T_{im} = 0.5$ (middle), $T_{end} = 1$ (bottom).

The solutions for pressure and water content for constant $K = K_S$ are given at $T_1 = 0.01$, $T_{im} = 0.5$ and $T_{end} = 1$ with $\tau = 0$, 20, $1 - \theta^2$ and $10^2 \times e^{-7.7\theta}$. The computations are performed with step size h, time step Δt and values of L_Ψ and L_θ as defined previously.

Figure 4.5 presents similar solutions as the ones displayed in Figure 4.4, but for non-constant $K(\theta)$. The different nonlinear functions of the dynamic effect coefficient $\tau(\theta)$ are based on experimentally determined models found in [42]. Recall that $\tau(\theta) = 0$ corresponds to the standard Richards equation not including any dynamic effects. By comparing the solutions of $\tau = 0$ in Figures 4.4 and 4.5 to the solutions in Figures 4.2 and 4.3 at each time, it is evident that this is indeed the case. For all values of τ, the increase as time evolves in pressure and water content are larger for constant than for non-constant hydraulic conductivity, K.

As mentioned previously this effects the transport of the dissolved component. The transport takes place through convection and diffusion of the substance, so by coupling the convection-diffusion equation to the flow equations, the numerical results shown in Figure 4.6 are obtained. The left figure displays the transport both in connection with the standard Richards equation and dynamic capillarity for constant $K = K_S$, while the figure on the right displays it for non-constant $K(\theta)$. The solutions are also for these given at time $T_1 = 0.01$, $T_{im} = 0.5$ and $T_{end} = 1$, $\tau = 20$.

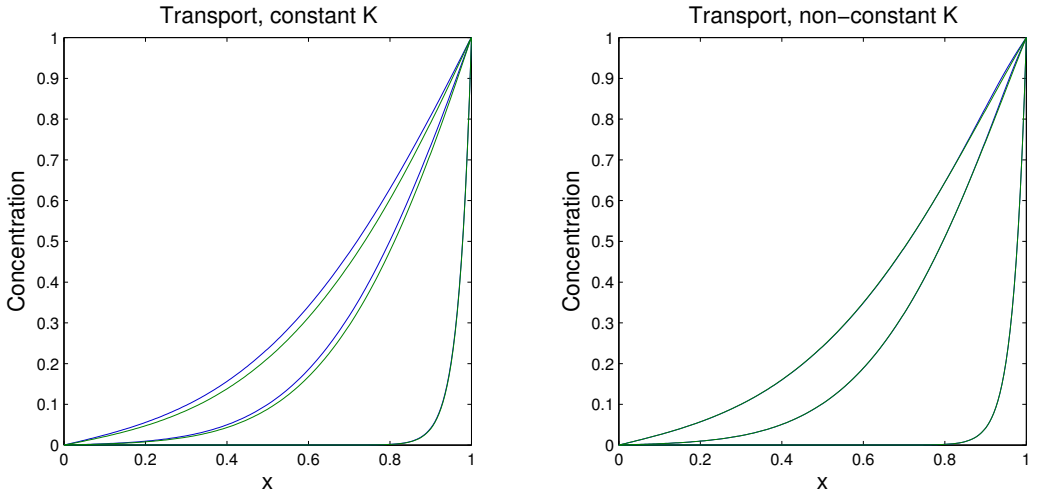

FIGURE 4.6: Transport profiles for standard Richards equation (blue solid line) and with dynamic capillary pressure (green solid line). The computations are done with constant $K = K_S$ (left) and non-constant $K(\theta)$ (right) at time $T_1 = 0.01$, $T_{im} = 0.5$, $T_{end} = 1$, $\tau = 20$.

For the case with constant K the dynamic effects are clear, portraying different transport profiles for the standard and non-standard model. In other words showing the effects of including dynamic capillary pressure in the model. However, when K is non-constant, the dynamic effects are hardly noticeable. This is mainly caused by the small change in water content, θ, for the non-constant case.

Recall from section 2.4.2 that coupling the convection-diffusion equation to the flow equations means that water content, θ, and volumetric flux, q, are obtained from the computations of Richards' equation. Assuming that the flux undergo little change during the simulations, the main influence on the transport is clearly caused by the water content.

The change in θ when comparing the standard and the non-standard model is small for the case with non-constant K (see figs. 4.3 and 4.5), thus accounting for the observed similarities in the transport profiles for the standard and non-standard model for non-constant $K(\theta)$. In a similar fashion, the bigger difference in θ for constant K accounts for the observed dynamic effects in this case.

Example II

The initial condition for the pressure Ψ is given by

$$\Psi(x, 0) = -1,$$

and is therefore a more physical example than the previous one, resulting in a constant pressure and water content profile at the initial time.

As in example I, numerical results are computed by implementing certain values of τ, defined above, in the scheme modelling dynamic effects. Recall that $L_\Psi = 0.001$ and $L_\theta = 1$. Together with the parameters and conditions defined at the start of the section, simulations are performed with step size $h = 0.005$ and time step $\Delta t = 0.01$.

Numerical solutions of pressure Ψ and water content θ for the different τ are given in Figures 4.7 and 4.8. Figure 4.7 show the solutions computed with constant $K = K_S$ and Figure 4.8 show the ones computed with non-constant $K(\theta)$. The solutions are given at $T_1 = 0.01$, $T_{im} = 0.5$ and $T_{end} = 1$. Again, as time evolves there is an increase in pressure and water content throughout the domain due to the flux across the left boundary. This is the case for all values of τ. The observed increase is higher for the case with constant K than non-constant K. However, when comparing these results to those in example I (figs. 4.4 and 4.5) the increase is less for constant K and slightly higher for non-constant K.

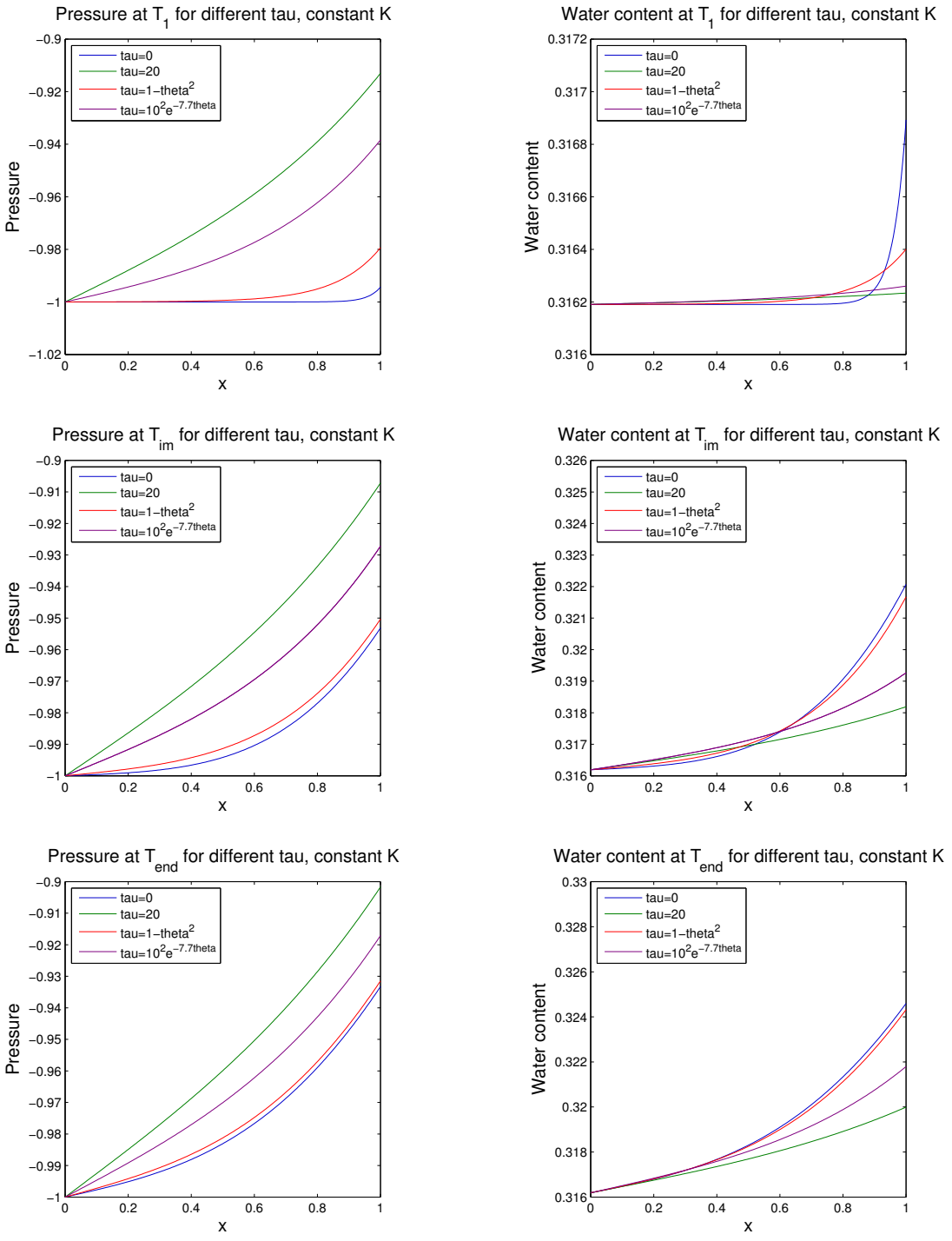

FIGURE 4.7: Pressure and water content profiles for different values of τ both constant and non-linear, $\tau = 0,\ 20,\ 1-\theta^2,\ 10^2 \times e^{-7.7\theta}$. Computations are done with constant $K = K_S$ at time $T_1 = 0.01$ (top), $T_{im} = 0.5$ (middle), $T_{end} = 1$ (bottom).

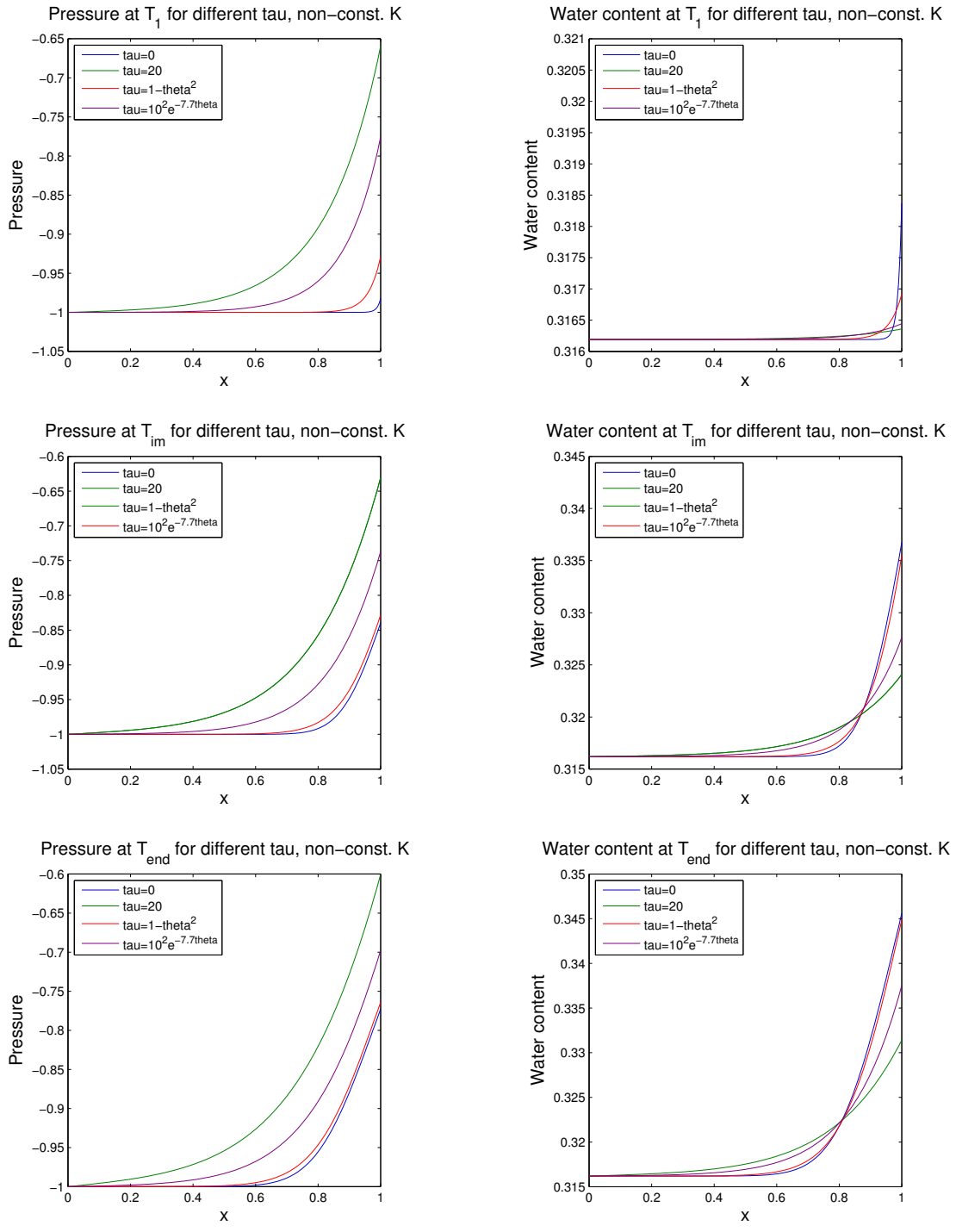

FIGURE 4.8: Pressure and water content profiles for different values of τ both constant and non-linear, $\tau = 0,\ 20,\ 1-\theta^2,\ 10^2 \times e^{-7.7\theta}$. Computations are done with non-constant $K(\theta)$ at time $T_1 = 0.01$ (top), $T_{im} = 0.5$ (middle), $T_{end} = 1$ (bottom).

In Figure 4.9 the transport profiles for the standard Richards equation as well as the non-standard equation, including dynamic capillarity, are given. The solutions for constant $K = K_S$ are shown in the figure on the left, while the solutions for the non-constant $K(\theta)$ are given by the figure on the right. As in Figure 4.6 the solutions are given at $T_1 = 0.01$, $T_{im} = 0.5$ and $T_{end} = 1$, $\tau = 20$.

Neither profile show a clear effect of including dynamic capillary pressure. This is manily due to the small change in water content θ (see Figures 4.7 and 4.8) as suggested previously.

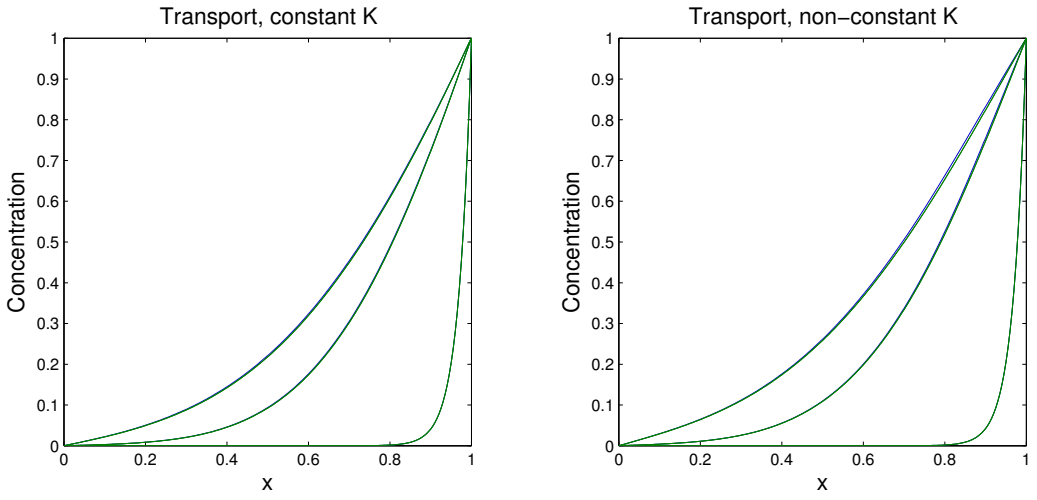

FIGURE 4.9: Transport profiles for standard Richards equation (blue solid line) and with dynamic capillary pressure (green solid line). The computations are done with constant $K = K_S$ (left) and non-constant $K(\theta)$ (right) at time $T_1 = 0.01$, $T_{im} = 0.5$, $T_{end} = 1$, $\tau = 20$.

4.2.2 Convergence History of the Linearisation Schemes

In this section numerical simulations for the academical example, section 4.1, and example I, section 4.2.1, are performed. However, the focus now lies on the convergence of the linearisation schemes introduced in section 3.4.

For all simulations a constant time step of 0.1 is used, and a tolerance in residual error of 10^{-4} for the non-linear system is given. A one dimensional grid with varying mesh size $h = 0.02$, 0.008 and 0.005 is considered.

Figure 4.10 illustrates the convergence of the academical example. It is clear that the linear error reduction factor is independent of mesh size, with four iterations needed to reach the tolerance, for any value of h.

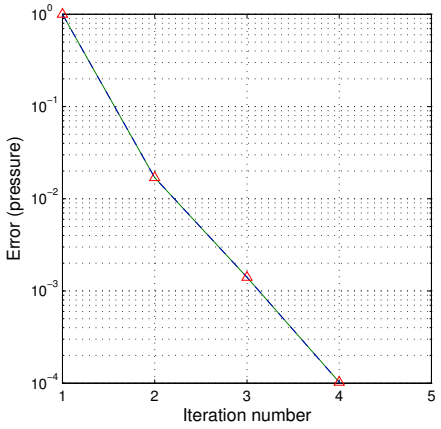

FIGURE 4.10: Convergence history of relative pressure error at $T_1 = 0.1$ for various mesh sizes for the academical example. Illustrated by $h = 0.02$ (green solid line), $h = 0.008$ (blue dashed line) and $h = 0.005$ (red triangles). With constant $\Delta t = 0.1$.

In Figure 4.11 the convergence for the standard Richards equation for constant $K = K_S$ and non-constant $K(\theta)$ is presented. For K constant no more than nine iterations are needed. This is depicted by the figure on the right. In the case with non-constant K, see the figure to the left, the negligible difference between $h = 0.02$ and $h = 0.008, 0.005$ results in a total of six iterations. Hence, the linearisation scheme's independence of mesh size is obvious when applied to the standard Richards equation.

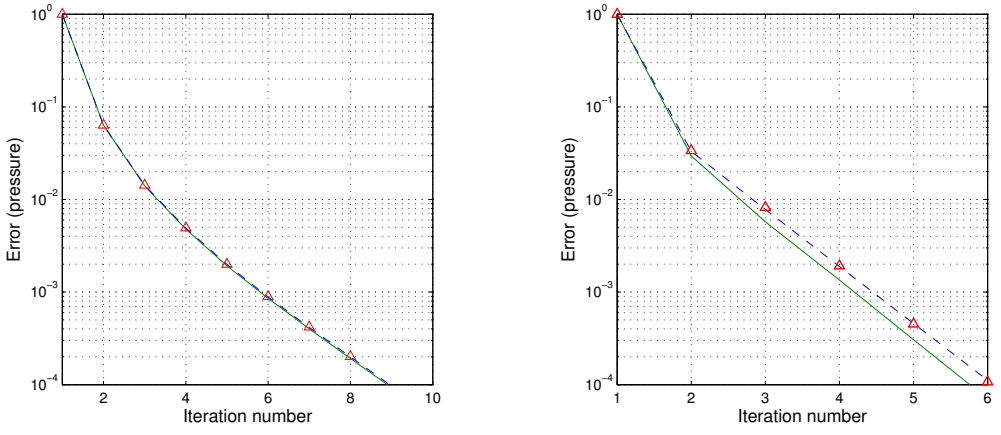

FIGURE 4.11: Convergence history of relative pressure error at $T_1 = 0.1$ for various mesh sizes for the standard Richards equation. Illustrated by $h = 0.02$ (green solid line), $h = 0.008$ (blue dashed line) and $h = 0.005$ (red triangles). Computations are done with constant $K = K_S$ (left) and non-constant $K(\theta)$ (right), $\Delta t = 0.1$.

Remark. In section 3.4.1 the convergence of the linearisation scheme for the standard Richards equation was given by the contraction

$$f(\cdot) = \frac{L}{L+\alpha} \leq 1,$$

where L is some Lipschitz constant and $\alpha \propto \Delta t a$ with a not depending on Δt (see (3.66), section 3.4.1). From this relation some restrictions on the choice of L, α arises, illustrated by taking the limits of the relation as $\lim_{L\to\infty} f(L)$ and $\lim_{\alpha\to 0} f(\alpha)$:

$$\lim_{L\to\infty} f(L) = \lim_{L\to\infty} \frac{L}{L+\alpha} = 1,$$
$$\lim_{\alpha\to 0} f(\alpha) = \lim_{\alpha\to 0} \frac{L}{L+\alpha} = 1.$$

In other words, the convergence will be very poor (or nonexisting) for L too big and/or a, Δt too small, implying a mild restriction on the time step size.

Figure 4.12 illustrates the rate at which the relations approaches 1. The figure on the left shows the rate approaching 1 when L increases and $\alpha = 0.01, 0.1, 1$, while the one on the right shows the rate approaching 1 when α decreases and $L = 0.1, 1, 10$.

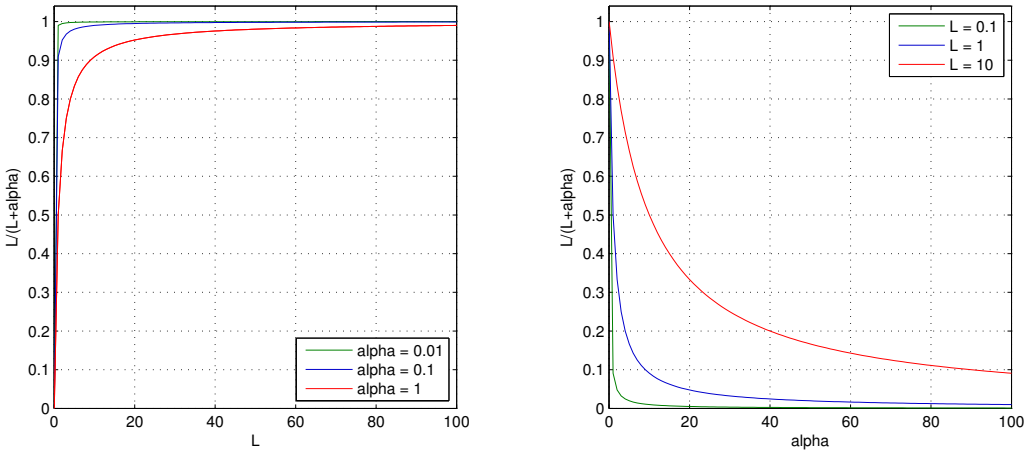

FIGURE 4.12: Rate of function $f = \frac{L}{L+\alpha}$ approaching 1 for L increasing (left) and α decreasing (right). Computed with $\alpha = 0.01$ (green line), $\alpha = 0.1$ (blue line) and $\alpha = 1$ (red line) for increasing L. Computed with $L = 0.1$ (green line), $L = 1$ (blue line) and $L = 10$ (red line) for decreasing α.

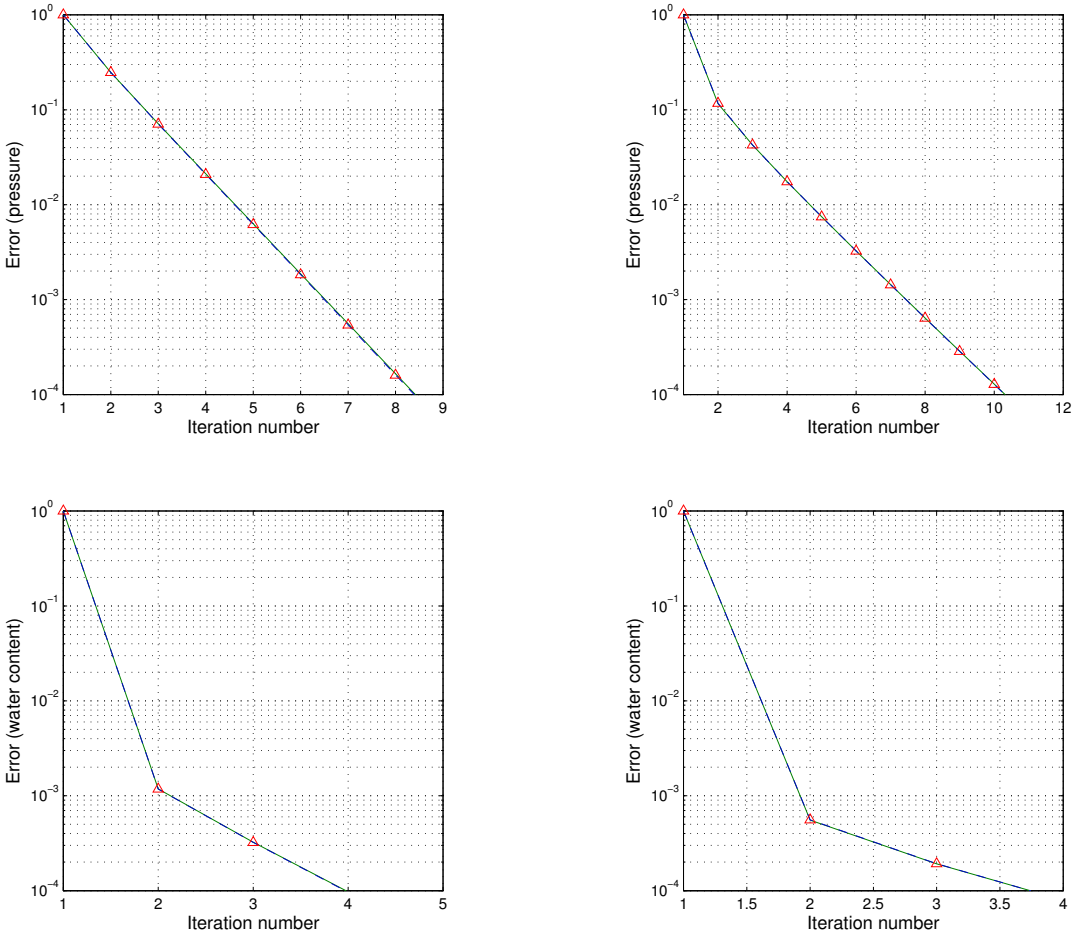

FIGURE 4.13: Convergence history of relative pressure error (top) and relative water content error (bottom) with dynamic capillary pressure, at $T_1 = 0.1$ for various mesh sizes. Illustrated by $h = 0.02$ (green solid line), $h = 0.008$ (blue dashed line) and $h = 0.005$ (red triangles). Computations are done with constant $K = K_S$ (left) and non-constant $K(\theta)$ (right), $\Delta t = 0.1$ and $\tau = 20$.

As in the case for the academical example and the standard Richards equation, the convergence of the linearisation scheme for Richards' equation with dynamic capillarity, where $\tau = 20$, is independent of h, see Figure 4.13. This is evident with regards to pressure as well as the water content. An increase in the number of iterations needed is observed for the pressure solution between constant $K = K_S$ and non-constant $K(\theta)$, while a slight decrease is observed for the water content. In Figure 4.14 the convergence with nonlinear $\tau = 1 - \theta^2$ is shown. With just over four iterations needed for the pressure and just over three for the water content for all values of h, this is also independent of mesh size. The convergence results presented so far in this section, verifies the robustness and generality of the iterative schemes as well as the suitability of the finite volume discretisation.

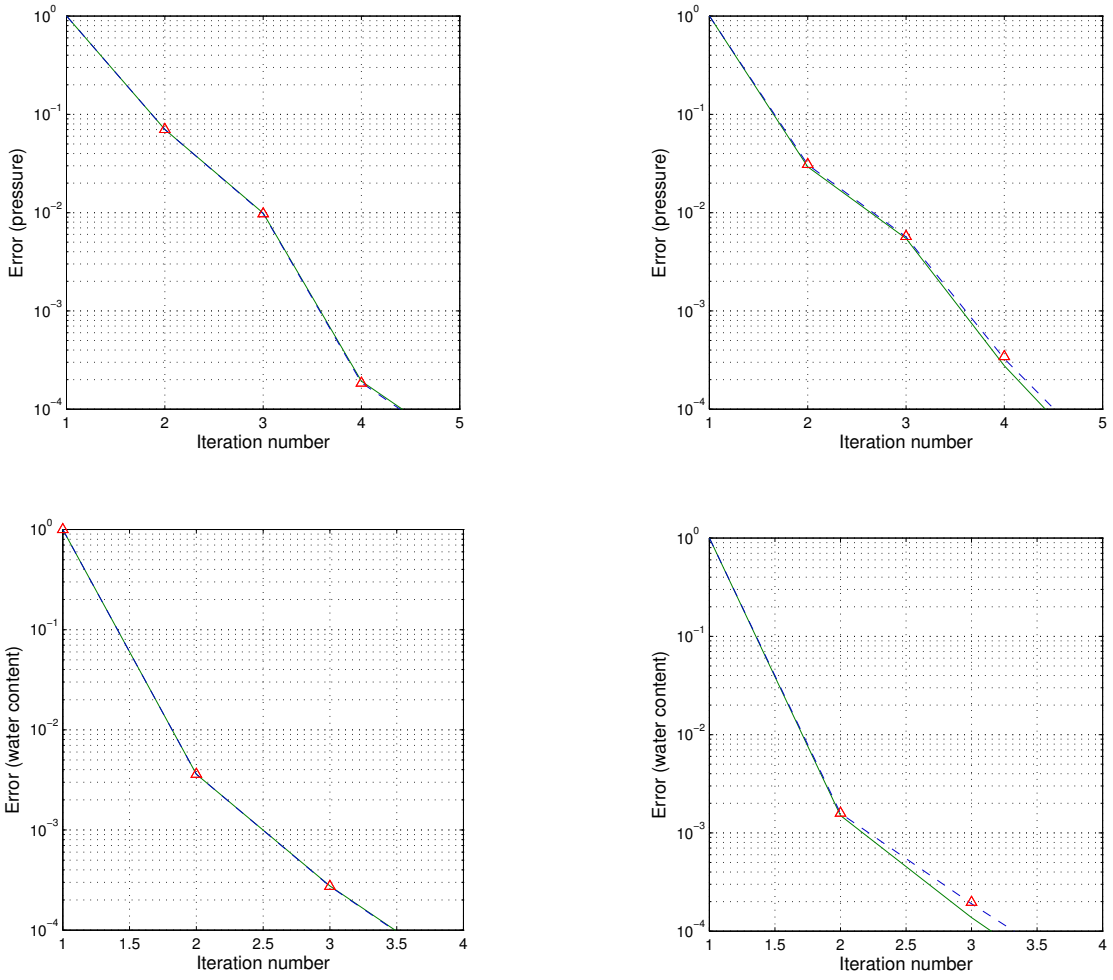

FIGURE 4.14: Convergence history of relative pressure error (top) and relative water content error (bottom) with dynamic capillary pressure, at $T_1 = 0.1$ for various mesh sizes. Illustrated by $h = 0.02$ (green solid line), $h = 0.008$ (blue dashed line) and $h = 0.005$ (red triangles). Computations are done with constant $K = K_S$ (left) and non-constant $K(\theta)$ (right), $\Delta t = 0.1$ and $\tau = 1-\theta^2$.

In order to further explore the robustness and generality of the linearisation schemes, the convergence history for different values of the dynamic effect coefficient τ is computed, see Figure 4.15. The computations were performed with $h = 0.005$. Throughout these numerical simulations, the error reduction factor is independent of grid size and no more than six iterations was needed.

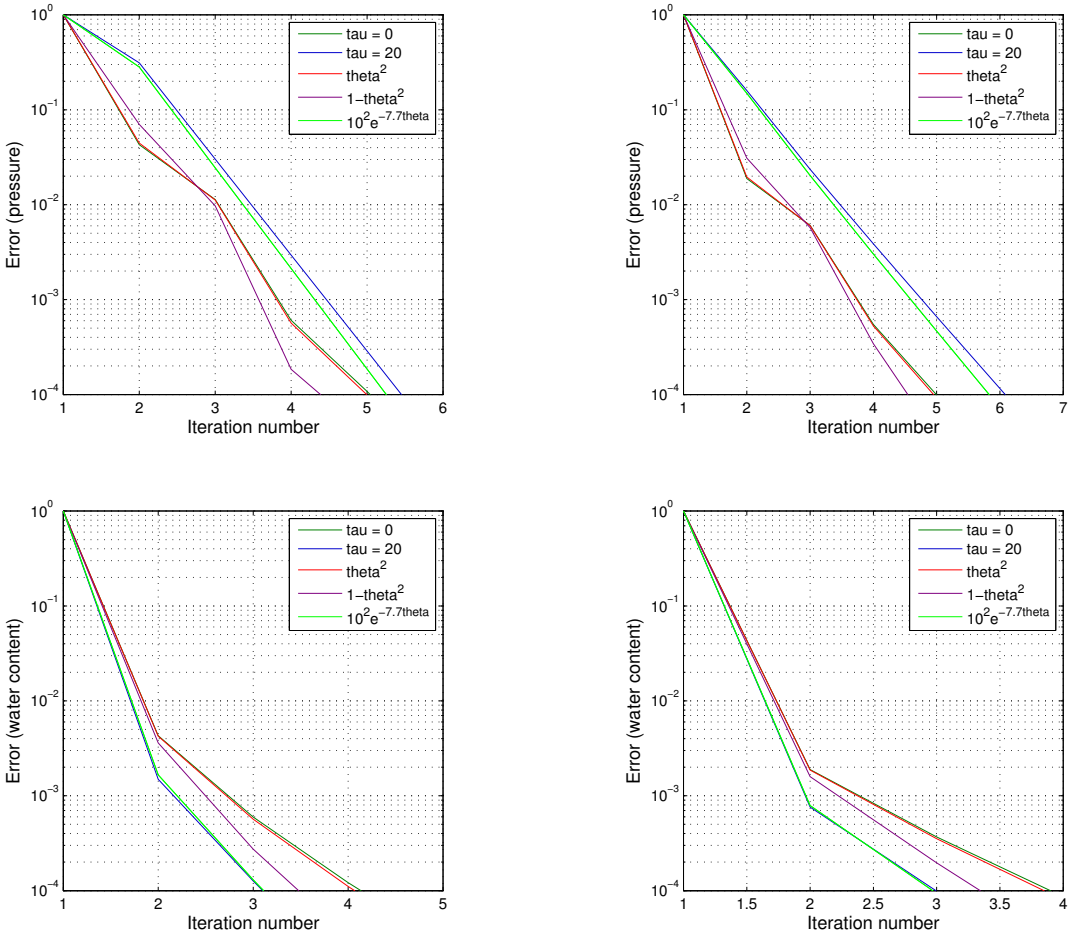

FIGURE 4.15: Convergence history of relative pressure error (top) and relative water content error (bottom), at $T_1 = 0.1$ for various values of τ. $\tau = 0$, 20, θ^2, $1-\theta^2$, $10^2 \times e^{-7.7\theta}$. Computations are done with constant $K = K_S$ (left) and non-constant $K(\theta)$ (right), $\Delta t = 0.1$ and $h = 0.005$.

Chapter 5

Conclusion

In this thesis dynamic capillary effects on numerical simulations of flow and transport in porous media have been considered. To do so, mathematical models to model flow and transport were constructed, given by the Richards equation and the convection-diffusion equation. In order to account for dynamic effects related to phenomena such as saturation overshoot and formation of preferential flow paths, an extension describing dynamic capillary pressure was included in the standard model, hence developing what was referred to as a non-standard model. The aim was thus to evaluate the influence of dynamic effects on the flow and transport of a dissolved substance.

Richard's equation admits in general no analytical solutions, hence numerical solutions have to be considered. In this thesis the discretisation in time was performed by using the backward Euler method and in space the cell-centered finite volume method TPFA. To solve the nonlinear systems appearing at each time step, robust linearisation methods were proposed. The scheme for the Richards equation with dynamic capillarity is new. The schemes were analysed to prove the convergence of the methods. All simulations were conducted using the Matlab implementation environment and the numerical simulations supported the evidence put forward by the theoretical analysis. The linearisation schemes are very robust, shown to be linearly convergent and independent of mesh diameter, which is an argument for the efficiency of the schemes. Another advantage of the presented schemes is that they do not involve the calculations of derivatives. The numerical scheme for the standard Richards equation, based on the works of *Slodicka* (2002) and *Pop and Radu* (2004) [37, 40], and the new scheme including the dynamic capillarity are relatively simple to implement and are valuable alternatives to Picard or Newton methods.

The numerical simulations of the flow and transport models were performed on two examples with different initial conditions. Numerical solutions based on the standard and the non-standard Richards equation were presented. In terms of the flow, the dynamic effect was evident and a clear difference between the solutions of the standard and non-standard case was seen. This was true for both the pressure, Ψ, and water content, θ. As well as computing numerical solutions to problems matching the theoretical analysis where constant K, $\tau > 0$ were assumed, numerical simulations were performed on problems containing non-constant K, τ, implying that similar characteristics also holds for such problems. This is however in the need of further exploration and a proper theoretical analysis should be established. Regarding the transport problem, dynamic effects were observed in the case with constant $K = K_S$ for Example I (see section 4.2.1). For the remaining transport computations, the chosen values and conditions resulted in a change in θ not significant enough to portray dynamic effects.

If time had allowed it, the model would be extended to include hysteresis as well as dynamic capillarity in an effort to obtain saturation overshoot profiles and further investigating the influence on the transport. Applying the implemented schemes to more realistic examples over longer time spans would hopefully result in solutions showing the true dynamic effects and underline the importance of including non-standard aspects in the model.

Bibliography

[1] J Bear and Y Bachmat. *Introduction to modeling of transport phenomena in porous media*, volume 4. Springer, 1990.

[2] JM Nordbotten and MA Celia. *Geological storage of CO2: modeling approaches for large-scale simulation*. John Wiley & Sons, 2011.

[3] Ø Pettersen. Grunnkurs i reservoarmekanikk. *Matematisk institutt-UIB*, 1990.

[4] Z Chen, G Huan, and Y Ma. *Computational methods for multiphase flows in porous media*, volume 2. Siam, 2006.

[5] P Knabner and L Angermann. *Numerical methods for elliptic and parabolic partial differential equations*. Springer, 2003.

[6] RA Adams and C Essex. *Calculus: a complete course*, volume 7. Addison-Wesley Don Mills, Ontario, 2009.

[7] PW Atkins and J De Paula. *The elements of physical chemistry*. Oxford University Press New York, NY, USA, 2005.

[8] JM Cooper. Introduction to partial differential equations with matlab birkhauser. *Boston, MA*, 1998.

[9] D DiCarlo. Stability of gravity-driven multiphase flow in porous media: 40 years of advancements. *Water Resources Research*, 49(8):4531–4544, 2013.

[10] R Khaleel, JF Relyea, and JL Conca. Evaluation of van genuchten–mualem relationships to estimate unsaturated hydraulic conductivity at low water contents. *Water Resources Research*, 31(11):2659–2668, 1995.

[11] JN Reddy. *An introduction to continuum mechanics*. Cambridge university press, 2007.

[12] J Aarnes, T Gimse, and K Lie. An introduction to the numerics of flow in porous media using matlab. In *Geometric Modelling, Numerical Simulation, and Optimization*, pages 265–306. Springer, 2007.

[13] FA Radu. Lecture notes on flow in porous medium (mat254), 2013.

[14] SS Mundal. Conservative numerical methods for elliptic problems with applications to simulation of near-well flow. 2009.

[15] S Costabel and U Yaramanci. Relative hydraulic conductivity in the vadose zone from magnetic resonance sounding—brooks-corey parameterization of the capillary fringe. *Geophysics*, 76(3):G61–G71, 2011.

[16] S Bottero. Advances in the theory of capillarity in porous media. *Geologica Ultraiectina*, 314, 2009.

[17] FJ-M Kalaydjian et al. Dynamic capillary pressure curve for water/oil displacement in porous media: Theory vs. experiment. In *SPE Annual Technical Conference and Exhibition*. Society of Petroleum Engineers, 1992.

[18] SM Hassanizadeh and WG Gray. Mechanics and thermodynamics of multiphase flow in porous media including interphase boundaries. *Advances in water resources*, 13(4):169–186, 1990.

[19] I Aavatsmark. Bevarelsesmetoder for elliptiske differensialligninger. *Studieretning beregningsvitenskap, UiB*, 2004.

[20] GJ Haltiner and RT Williams. *Numerical prediction and dynamic meteorology*, volume 2. Wiley New York, 1980.

[21] JW Thomas. *Numerical partial differential equations: finite difference methods*, volume 22. Springer, 1995.

[22] Y Fan and IS Pop. A class of pseudo-parabolic equations: existence, uniqueness of weak solutions, and error estimates for the euler-implicit discretization. *Mathematical Methods in the Applied Sciences*, 34(18):2329–2339, 2011.

[23] I Aavatsmark. Interpretation of a two-point flux stencil for skew parallelogram grids. *Computational geosciences*, 11(3):199–206, 2007.

[24] A Quarteroni, R Sacco, and F Saleri. *Numerical mathematics*, volume 37. Springer, 2007.

[25] DR Kincaid and EW Cheney. *Numerical analysis: mathematics of scientific computing*, volume 2. American Mathematical Soc., 2002.

[26] I Danaila, P Joly, SM Kaber, and M Postel. *An introduction to scientific computing, Twelwe Computational Projects Solved with MATLAB*. Springer, 2007.

[27] FA Radu, JM Nordbotten, IS Pop, and K Kumar. A robust linearization scheme for finite volume based discretizations for simulation of two-phase flow in porous media. 2014.

[28] MG Edwards. Unstructured, control-volume distributed, full-tensor finite-volume schemes with flow based grids. *Computational Geosciences*, 6(3-4): 433–452, 2002.

[29] MG Edwards and CF Rogers. Finite volume discretization with imposed flux continuity for the general tensor pressure equation. *Computational Geosciences*, 2(4):259–290, 1998.

[30] RA Klausen, FA Radu, and GT Eigestad. Convergence of mpfa on triangulations and for richards' equation. *International journal for numerical methods in fluids*, 58(12):1327–1351, 2008.

[31] IS Pop, M Sepúlveda, FA Radu, and OP Vera Villagrán. Error estimates for the finite volume discretization for the porous medium equation. *Journal of Computational and Applied Mathematics*, 234(7):2135–2142, 2010.

[32] FA Radu, IS Pop, and P Knabner. On the convergence of the newton method for the mixed finite element discretization of a class of degenerate parabolic equation. *Numerical Mathematics and Advanced Applications*, pages 1194–1200, 2006.

[33] FA Radu and IS Pop. Newton method for reactive solute transport with equilibrium sorption in porous media. *Journal of computational and applied mathematics*, 234(7):2118–2127, 2010.

[34] FA Radu and IS Pop. Mixed finite element discretization and newton iteration for a reactive contaminant transport model with nonequilibrium sorption: convergence analysis and error estimates. *Computational Geosciences*, 15(3): 431–450, 2011.

[35] L Bergamaschi and M Putti. Mixed finite elements and newton-type linearizations for the solution of richards' equation. *International journal for numerical methods in engineering*, 45(8):1025–1046, 1999.

[36] IS Pop, F Radu, and P Knabner. Mixed finite elements for the richards' equation: linearization procedure. *Journal of computational and applied mathematics*, 168(1):365–373, 2004.

[37] M Slodicka. A robust and efficient linearization scheme for doubly nonlinear and degenerate parabolic problems arising in flow in porous media. *SIAM Journal on Scientific Computing*, 23(5):1593–1614, 2002.

[38] FA Radu and W Wang. Convergence analysis for a mixed finite element scheme for flow in strictly unsaturated porous media. *Nonlinear Analysis: Real World Applications*, 15:266–275, 2014.

[39] SM Hassanizadeh, MA Celia, and HK Dahle. Dynamic effect in the capillary pressure–saturation relationship and its impacts on unsaturated flow. *Vadose Zone Journal*, 1(1):38–57, 2002.

[40] FA Radu. Mixed finite element discretization of richards' equation: error analysis and application to realistic infiltration problems. *University of Erlangen-Nürnberg, Heidelberg, Germany*, 2004.

[41] FA Radu. Convergent mass conservative schemes for flow and reactive solute transport in variably saturated porous media. 2013.

[42] R Fučík and J Mikyška. Numerical investigation of dynamic capillary pressure in two-phase flow in porous medium. *Mathematica Bohemica*, 136(4):395–403, 2011.

[43] E Schneid. Hybrid-gemischte finite-elemente-diskretisierung der richards-gleichung. *University of Erlangen-Nürnberg, Heidelberg, Germany*, 2004.